

# Finding the Cell Center by a Balance of Dynein and Myosin Pulling and Microtubule Pushing: A Computational Study

Jie Zhu,\* Anton Burakov,<sup>†</sup> Vladimir Rodionov,<sup>‡</sup> and Alex Mogilner\*

\*Department of Neurobiology, Physiology, and Behavior and Department of Mathematics, University of California–Davis, Davis, CA 95616; <sup>†</sup>A. N. Belozersky Institute of Physico-Chemical Biology, Moscow State University, Moscow 119899, Russia; and <sup>‡</sup>Department of Cell Biology and Center for Cell Analysis and Modeling, University of Connecticut Health Center, Farmington, CT 06032

Submitted July 27, 2010; Revised October 5, 2010; Accepted October 19, 2010  
Monitoring Editor: Thomas D. Pollard

The centrosome position in many types of interphase cells is actively maintained in the cell center. Our previous work indicated that the centrosome is kept at the center by pulling force generated by dynein and actin flow produced by myosin contraction and that an unidentified factor that depends on microtubule dynamics destabilizes position of the centrosome. Here, we use modeling to simulate the centrosome positioning based on the idea that the balance of three forces—dyneins pulling along microtubule length, myosin-powered centripetal drag, and microtubules pushing on organelles—is responsible for the centrosome displacement. By comparing numerical predictions with centrosome behavior in wild-type and perturbed interphase cells, we rule out several plausible hypotheses about the nature of the microtubule-based force. We conclude that strong dynein- and weaker myosin-generated forces pull the microtubules inward competing with microtubule plus-ends pushing the microtubule aster outward and that the balance of these forces positions the centrosome at the cell center. The model also predicts that kinesin action could be another outward-pushing force. Simulations demonstrate that the force-balance centering mechanism is robust yet versatile. We use the experimental observations to reverse engineer the characteristic forces and centrosome mobility.

## INTRODUCTION

Position and orientation of the nucleus (Burke and Roux, 2009), membrane organelles (Wada and Suetsugu, 2004), and mitotic spindles (Grill *et al.*, 2001) in cells are of crucial importance for their function in health and disease. Similarly, centrosome (CS) localization is essential for neural and epithelial differentiation, cell polarization, spindle positioning, and orientation and control of cell migration (Manneville and Etienne-Manneville, 2006). What are the mechanisms governing these phenomena is a fundamental question of cellular organization. Broadly, three factors—feedback in the reaction–diffusion signaling mechanisms, architectural heterogeneity of the cell, and cytoskeleton network mechanics—can be responsible for the spatial organization of the cell (Mullins, 2010). Here, we investigate the particular question of how the CS finds the cell center, in which the third factor, cytoskeletal mechanics, is crucial.

This article was published online ahead of print in *MBoC in Press* (<http://www.molbiolcell.org/cgi/doi/10.1091/mbc.E10-07-0627>) on October 27, 2010.

Address correspondence to: Alex Mogilner ([mogilner@math.ucdavis.edu](mailto:mogilner@math.ucdavis.edu)).

Abbreviations used: CS, centrosome; MT, microtubule.

© 2010 J. Zhu *et al.* This article is distributed by The American Society for Cell Biology under license from the author(s). Two months after publication it is available to the public under an Attribution–Noncommercial–Share Alike 3.0 Unported Creative Commons License (<http://creativecommons.org/licenses/by-nc-sa/3.0>).

In many cell types, the CS in interphase is found at the centroid or geometric center of the cell (Dujardin and Vallee, 2002). CS is the focal point of microtubule (MT) aster, so it is not surprising that MTs play a key role in the CS centering, because their length approaches that of the whole cell and also because their rapid growth and shortening dynamics allow them to explore the entire cell space (Wühr *et al.*, 2009). The ability of MTs growing against an obstacle to generate pushing forces by polymerization ratchet mechanism (Dogterom and Yurke, 1997) is at the core of the MT aster centering in vitro (Holy *et al.*, 1997): if the aster's focal point is closer, for example, to the left edge of the experimental chamber (see Figure 1A), then shorter MTs at that side grow against the boundary and buckle. Mechanically, MT filaments are elastic rods, and their buckling forces are inversely proportional to the square of their lengths. Thus, at the left, short MTs buckling against the boundary push the aster to the right with a significant force, whereas at the right fewer MTs reach the boundary because of the periodic shortening, and those that do reach the boundary are long and buckle at a weaker force. The resulting imbalance of the pushing forces drives the MT aster to the central position. This elegant MT pushing mechanism also works in vivo: in the small fission yeast cells, the nucleus can be centered by pushing forces that are generated when growing MTs hit the cell edges (Tran *et al.*, 2001; Tolić-Nørrelykke *et al.*, 2004). The growing MTs also can push against barriers scattered throughout the cytoplasm, such as yolk granules (Bjerknes, 1986; Wühr *et al.*, 2009) in some cells, but the respective mechanical effect was never studied.

Typically, however, the forces in the cell are generated not by MTs directly but by the host of molecular motors using the MTs as tracks (Civelekoglu-Scholey and Scholey, 2010). There are many examples of pulling motor forces positioning cell structures (Grill *et al.*, 2001; Pearson and Bloom, 2004). The most well known of them occurs in *Caenorhabditis elegans* eggs where dyneins associated with the actin cortex at the cell boundary through dynactin, attempt to move toward the MT minus-ends, thereby generating pulling forces on MTs reaching the cell cortex (Grill and Hyman, 2005; see Figure 1B). At first glance, this pulling mechanism should be destabilizing (see Figure 1B): if the aster's focus is closer to the left, more filaments will reach the cortex there, and the force pulling to the left will be stronger decentering the aster. However, if the number of pulling dyneins is limiting, while an abundant number of MTs reach the cortex at all sides of the cell, then this mechanism, in which the motors pull on the MT plus-ends, becomes centering (Grill and Hyman, 2005).

Another possibility is for the dynein motors to be distributed throughout the cytoplasm and attached to structures not easily displaced, e.g., endoplasmic reticulum, yolk, intermediate filaments, or actin (Reinsch and Gönczy, 1998). Then, the longer the MT, the more motors it can engage along its length, leading to a length-dependent pulling force. This servomechanism proposed in Hamaguchi and Hiramoto (1986) (for review, see Dujardin and Vallee, 2002) should stabilize the centering: the aster experiences a net force in the direction of the longest MTs and thus toward the center of the cell (see Figure 1C). The necessary interactions of dyneins with lateral MT surface were observed in fission yeast (Vogel *et al.*, 2009), budding yeast (Adames and Cooper, 2000), and *Dictyostelium* cells (Koonce and Khodjakov, 2002). For this mechanism to work, the force generators have to be distributed uniformly in the cytoplasm. In many cells, this cannot be the case, because many motors are localized to the dense, yet thin, actin layer of the cell cortex underlying the plasma membrane, whereas the cell interior has vast regions with large fluid fraction of the cytoplasm that the motors are unlikely to fasten to. However, in flat cells, the cortex is close to any point in the interior, and MTs can align along the cortex and thus experience cortical length-dependent forces (O'Connell and Wang, 2000) and get engaged in the servomechanism. Note also that although dynein, anchored to the cortex via dynactin, is the most prominent candidate for forcing MTs (Dujardin and Vallee, 2002), kinesins enmeshed into the actin-rich cortex also can engage MTs at or near their ends and push on them (Brito *et al.*, 2005).

Last but not least, MTs interact with actin gel mechanically through molecular complexes that can simultaneously associate with actin and MT filaments (Huang *et al.*, 1999; Kodama *et al.*, 2003; Weber *et al.*, 2004). Myosin-powered contraction causes ubiquitous centripetal flow of F-actin in cells (Yam *et al.*, 2007; Alexandrova *et al.*, 2008). MTs that are coupled to this flow are dragged and transported to the center (Mikhailov and Gundersen, 1995; Yvon and Wadsworth, 2000; Salmon *et al.*, 2002; Rosenblatt *et al.*, 2004; see Figure 1D). In addition, MTs can be pulled by myosin motors directly on actin cables (Hwang *et al.*, 2003).

Here, we focus on the phenomenon of the CS centering in flat mammalian tissue culture cells in the interphase. Our experimental study (Burakov *et al.*, 2003) revealed that dynein motors' pulling on MTs is responsible for the force stabilizing the CS at the cell center. This force is assisted by a myosin-dependent centering force. The latter is not strong enough to stabilize the symmetric MT aster position by itself

due to the third factor that destabilizes the aster and moves the CS to the cell edge. This third factor is associated with the MT turnover dynamics, because using Taxol to stabilize MTs nullifies the respective force. The nature of this MT dynamics-dependent anticentering force, however, remains unknown.

Mathematical and computational modeling was used extensively to complement traditional cell biological and biophysical methods to elucidate mechanistic details of the centering mechanisms in several systems (Holy *et al.*, 1997; Grill *et al.*, 2001; Vogel *et al.*, 2009). Modeling is especially useful because individual MTs and motors are next to impossible to resolve microscopically in many systems and because measuring forces directly is too difficult. Here, we use the reverse engineering approach that has been successfully applied to cytoskeletal mechanics problems (Wollman *et al.*, 2008; Foethke *et al.*, 2009), and we use the observations and measurements reported in Burakov *et al.* (2003) to answer the following questions: Do dyneins pull on the MT plus-ends or along their length? What is the nature of the anticentering force? How many motors and MTs are involved and what are the characteristic forces in the centering mechanism?

## MATERIALS AND METHODS

### Modeling

We developed both a continuous deterministic model and a discrete stochastic model in which the flat cell is represented as a disk of  $\sim 20 \mu\text{m}$  in radius that can be gleaned from the microscopic images. In the continuous model, we place the CS at a distance  $x$  from the cell center; from the symmetry considerations, the net force applied to all MTs on the CS is directed along the  $x$ -axis toward the cell center (see Figure 2A). We consider an individual MT (Figure 2A) and three forces applied to it: a pushing force  $f_{push}$ , acting on its plus-end and directed toward the minus-end, a dynein force  $f_{dyn}$  pulling the MT side and directed toward the plus-end, and an actin-flow-induced drag force  $f_{act}$  pulling the MT toward the cell center. The elementary dynein and pushing forces are constant, while the actin drag force increases from the center to the edges of the cell because actin flow decelerates from the periphery to the center of the cell. We integrate the dynein and actin forces along the length of each MT and then integrate the results over all the MTs to get the total force on the CS as described in Supplemental Material. When integrating, we assume that there are a constant number of motors per MT unit length, that the motor forces are additive, and that the force per motor is independent of the MT movement. The last two assumptions are justified because MTs move much slower than free dyneins glide, so that each dynein motor operates near its stall force. In the continuous model, we assume that the MT aster is radially symmetric about the CS. We use the dynamic instability theory (Dogterom and Leibler, 1993) to find the steady-state continuous distribution of MT plus-ends that is used in the integration. When the nocodazole is applied to the cell locally, we assume that any MT reaching for the edge of the nocodazole-affected field undergoes a catastrophe and that there are no MTs in the wedge shown in Figure 2E. We repeat all the described calculations for the elliptical and one-dimensional (1D) cells. We also consider hypothetical kinesin forces along the MT length and dynein forces from the cell boundary. Respective mathematics is described in Supplemental Material.

Because the number of MTs estimated from the experiment is on the order of 100 and the known dynamic instability time scale is less than an order of magnitude faster than the characteristic time scale of the CS's movement, the stochastic effects also should be considered. Thus, we developed a discrete stochastic model to verify the results of the continuous model and to make a visual presentation of the model simulations resulting in Supplemental Movies 1–5. In the stochastic model, individual MTs and their dynamic instability are treated explicitly as described in Paul *et al.* (2009). As described in Supplemental Material, MTs are nucleated at the CS at a constant rate. At each time step, they grow or shorten with fixed speeds. The transitions between the growing and shortening states take place randomly with observed constant catastrophe and rescue rates. At each time step, the force on each MT is calculated numerically according to the formulae from the continuous model, and the forces from all the current MTs are summated to obtain the total force on the CS. The CS is then displaced according to the equation  $d\bar{x}/dt = \mu F$  (Civelekoglu-Scholey and Scholey, 2010), where  $\bar{x}$  is the CS's coordinate in two dimensions,  $F$  is the total current force on the CS, and  $\mu$  is the CS's mobility. Preliminary estimates showed that making the model fully stochastic and introducing random flickering on and off in the forces do not qualitatively change the results.

## Experiment

Images displayed in Figures 4 and 5, CS movement rates, MT dynamic instability parameters, and cell dimensions used to develop and calibrate the quantitative model are obtained as described in detail in Burakov *et al.* (2003).

## RESULTS

### Qualitative Analysis Suggests That MT Pushing on Obstacles throughout the Cortex Destabilizes the CS Positioning

Our model is based on the following observations (Burakov *et al.*, 2003). 1) When dynein is inhibited, centering is destabilized and the CS moves away from the center (Figure 2B, red arrow). 2) Inhibition of myosin stops the centripetal actin flow but does not affect the centering (Figure 2C, green arrow illustrates the CS centering). 3) When both dynein and myosin are inhibited, the CS moves away from the center. 4) When dynein is inhibited, and in addition the cell is treated with Taxol inhibiting MT dynamics, the CS stays at the center (Figure 2D, green arrow illustrates the CS centering). 5) When nocodazole is applied locally to the cell edge disrupting MTs there, the CS shifts away from the center *toward* the nocodazole source (Figure 2E, green arrow). 6) When nocodazole is applied locally, and in addition myosin is inhibited in the cell, the CS shifts *away* from the nocodazole source (Figure 2F, red arrow). 7) Finally, when nocodazole is applied locally, together with myosin inhibition and dynein weakening, the CS oscillates near the cell center.

These results indicate that three mechanisms participate in CS positioning: one mechanism is dynein dependent; another mechanism is myosin powered; and the third mechanism relies on the MT dynamics, meaning that either growing or shortening MT plus-ends are involved. Result 1 indicates that dynein's action is to stabilize the CS at the center, probably by pulling astral MTs along their length, because pulling only from the cell boundary would destabilize the centering. In Supplemental Material, we provide calculations showing that the centering effect of a limited dynein number pulling from the cell boundary is less likely. The reason is that when nocodazole is applied locally, dynein from the unaffected part of the cell boundary reorients the pulling force so effectively that the CS is likely to be shifted away from the nocodazole source contradicting experimental result 5. Result 4 that deals with the situation, in which the dynein- and MT dynamics-related forces are suppressed and only the myosin-generated force acts (Figure 2D), indicates that the myosin-powered mechanism is also to stabilize the CS at the center. Probably, the interaction is through transient associations between the MTs and the centripetally flowing F-actin, which causes effective inward drag force on the MTs. Result 3 associates the destabilizing mechanism with the MT dynamics. Results 1 and 2 also hint that the dynein-dependent centering is stronger than the destabilizing mechanism, whereas the myosin-dependent centering is weaker.

Plausible positioning mechanisms based on the MT dynamics could result from the interactions between MT plus-ends and cell boundary or obstacles, or kinesin motors that are anchored throughout the cortex. Lateral interactions along the sides of MTs are less likely to contribute because such interactions do not require MT dynamic instability. However, under Kinesin Pushing along the MT Lengths Can Generate the Decentering Force, we discuss a possibility that the off-centering force originates from kinesin motors' pushing along the MT length (Figure 1F). If some motors pull on the MT plus-ends throughout the cytoplasm (or shortening MTs pull on cortex structures that remain attached to the

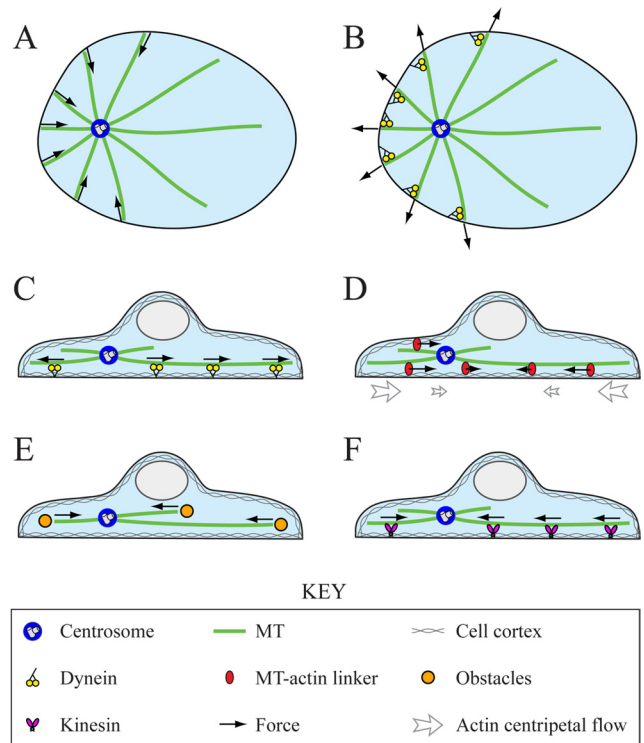


**Figure 1.** Hypothesized force-generation mechanisms. Top (A and B) and side (C–F) views of the cell. (A) MT pushing against the cell periphery stabilizes the CS centering because if the CS is closer to the left edge, more MTs will reach this edge and push the CS to the right. (B) Dynein pulling from the cell periphery destabilizes the CS centering, if the MT number is the limiting factor. (C) Dynein pulling on the MT sides stabilizes the CS at the center because if the CS is closer to the left edge, more motors will interact with the longer MTs at the right and pull the CS to the right. (D) Actin centripetal flow stabilizes the CS at the center because the dense MTs near the CS shift to the left, from where they are dragged toward the center by the flow. (E) Growing MT plus-ends' pushing against obstacles in the cytoplasm destabilizes the centering, because more MT plus-ends are oriented toward the distal cell edge. (F) Kinesin pushing on the MT sides destabilizes the CS because if the CS is closer to the left edge, more motors will interact with the longer MTs at the right and push the CS to the left.

MTs; Grishchuk *et al.*, 2005), they would stabilize the aster at the center because more growing plus-ends would be located between the CS and the distal side of the cell. Polymerizing MT plus-ends pushing on the cell boundary would lead to centering (Figure 1A), as discussed in the Introduction. One additional possibility is that when the CS is closer to one side of the cell, the MTs reorient such that they push the cell boundary only at the distal side, causing destabilization (Supplemental Figure S7). But in this case, the myosin-powered drag is also destabilizing (Supplemental Figure S7), which contradicts experimental result 4. If some motors pull the growing MT plus-ends from the cell boundary, they would destabilize the aster (Figure 1B). But this would contradict experimental result 7: MTs remaining on the opposite side of the nocodazole-application region would directly pull the CS toward that side, because myosin activity is inhibited. This leaves us with the only plausible mechanism: the growing MT plus-ends push on structures that are associated with the cortex, which lines up both the ventral and dorsal surfaces of the cell (Figure 1E). The following math-

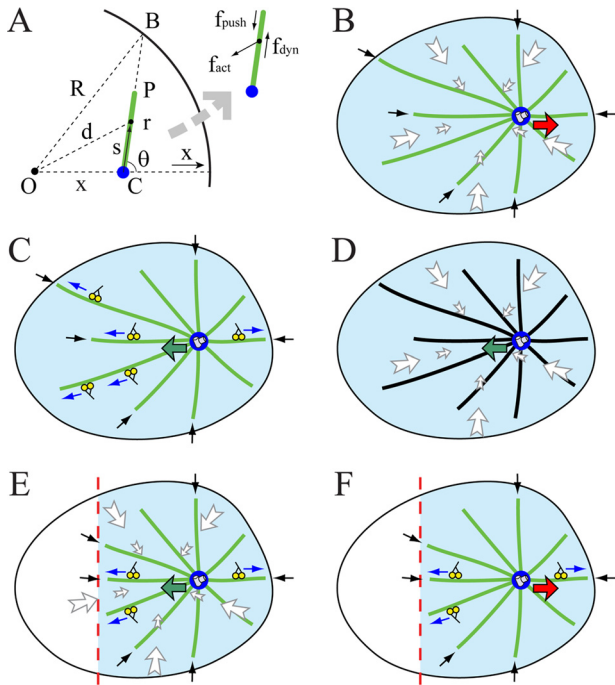


**Figure 2.** Geometry of the force generation. (A) Three principal forces on a single MT (green line) of length  $r$  in the cell with radius  $R$ : length-dependent force  $f_{dyn}$  by outward-pulling dyneins, flow- and length-dependent force  $f_{act}$  generated by the centripetal actin drag, and inward pushing force  $f_{push}$ . CS (blue) is displaced from the cell center by  $x$ .  $O$ ,  $C$ ,  $P$ ,  $B$ ,  $d$ ,  $s$ , and  $\theta$  are the geometric variables characterizing MT position and orientation used for force calculations in the Supplemental Material. (B) Perturbation (i): When dynein is inhibited and only actin drag and dynamic MT forces are present, centering is destabilized and the CS moves away from the center. (C) Perturbation (ii): When myosin is inhibited, the actin flow stops and only dynein and dynamic MT forces are present; the CS is stabilized at the center. (D) Perturbation (iv): When both dynein is inhibited and MTs are stabilized by Taxol, the actin flow stabilizes the CS at the center. (E) Perturbation (v): After the local application of nocodazole (modeled by eliminating MTs from the wedge of the cell), the CS shifts toward this wedge. (F) Perturbation (vi): After the local application of nocodazole and inhibition of myosin, the CS shifts away from the wedge. Green arrows, the CS is stabilized and moves toward the center; red arrows, the CS is destabilized and moves away from the center; blue arrows, pulling dynein forces; white arrows, actin–myosin drag forces; and black arrows, decentering forces associated with dynamic MTs. Dynamic MTs are shown in green, and Taxol-treated stable MTs are shown in black.

emathical model and simulations demonstrate that this hypothesis agrees with all the observations.

### Force Balance at the Centrosome Has Centering Effect If the Dynein Pulling Is Strong

We computed three major forces acting on the CS as functions of the distance from the center of a disk-like cell (Figure 3A). Confirming the qualitative analysis, Figure 3A (dotted) shows that when the CS shifts to the right from the center, then positive net force from MT pushing will move the CS further to the right, whereas negative net forces from dynein pulling and actin drag (solid and dashed, respectively) will return the CS to the center. Note that for each MT, dynein is pulling in the outward direction, whereas myosin is pulling inward. So, the elementary forces applied to individual MTs are in different directions and have dif-

ferent signs. However, after integrating the elementary forces over all the MTs, both (dynein and myosin) net forces act inward and therefore are stabilizing. Magnitudes of all three (dynein, myosin, and pushing) forces increase in a roughly linear manner as the CS shifts away from the center. This prediction agrees with the observation that the CS accelerates away from the center when dynein is inhibited (Burakov *et al.*, 2003). The calculation suggests that the sum of the three forces will have the centering effect if the net dynein-force is strong enough (density of dynein motors exceeds a threshold). Similarly, in absence of dynein, if the net force from myosin is less than that from MTs' pushing, the CS will be destabilized and will move to the cell edge.

We found the balance of CS in a cell to be determined by three characteristic forces:  $f_{push}$ , the average pushing force per MT;  $aL$ , the average dynein force per MT, and  $bL^2$ , the average myosin-driven force per MT. Here,  $L$  is the length scale for MT dynamics instability (see Supplemental Material),  $a$  is the dynein force per unit length of MT, and  $b$  is the characteristic actin drag-force per unit area. Note that parameter  $L$  predicted by the model (see Supplemental Material) is on the order of  $60 \mu\text{m}$ , whereas the cell radius is  $\sim 20 \mu\text{m}$ . This means that most MTs reach the cell boundary, which is observed, and most individual MTs are  $\sim 20 \mu\text{m}$  in length. The parameter scan (see below) suggests that when the relations  $aL \approx 3f_{push}$  and  $bL^2 \approx 8f_{push}$  are satisfied between these three main force scales, the total force on the CS becomes negative on the right side of the cell (Figure 3B, solid) and thus stabilizes the CS at the center against mechanical fluctuations. When myosin is inhibited, the sum of the net forces from dynein and MT-pushing remains negative (Figure 3B, dotted), so the centering persists. However, when either dynein alone (Figure 3B, dashed) or both dynein and myosin (Figure 3B, dot-dashed) are inhibited, the force becomes positive and the centered position of the CS is destabilized. Stochastic simulations depicted in Supplemental Movies 1 and 2 confirm these predictions. Simulations also demonstrate that away from the center the destabilized CS in the dynein-inhibited cell moves at a speed of the order of  $0.1 \mu\text{m}/\text{min}$ , in agreement with the data reported in Burakov *et al.* (2003). Snapshots from Supplemental Movies 1 and 2 mimicking the respective experimental images are shown in Figure 4.

### The Centrosome Undergoes a Small Shift from the Center If the MTs Are Spatially Perturbed

We modeled the local nocodazole application reported in Burakov *et al.* (2003) by calculating changes in the three major forces after deletion of MTs from the wedge at the cell side (Figures 2, E and F, and 5) and calculating respective changes in the three major forces. Supplemental Figure S3 illustrates how the forces change: after the MT density diminishes at the left, dynein pulls the CS to the right, so the dynein force becomes more positive in attempt to shift the CS to the right (Supplemental Figure S3A). However, two other forces have the opposite effect: more MTs at the right are dragged by the actin flow in the left direction (Supplemental Figure S3B). The pushing from the plus-ends of these dominating MTs also moves the CS to the left (Supplemental Figure S3C). Thus, despite the fact that dynein is stronger than either myosin or MT pushing separately, now that both the myosin-powered flow and the MT pushing oppose the dynein force, the net effect is shifting the CS to the left toward the nocodazole source. This is confirmed by Figure 3C (solid), which shows the net force on the CS in the presence of the nocodazole effect with parameter values satisfying  $aL \approx 3f_{push}$  and  $bL^2 \approx 8f_{push}$ . This force–distance

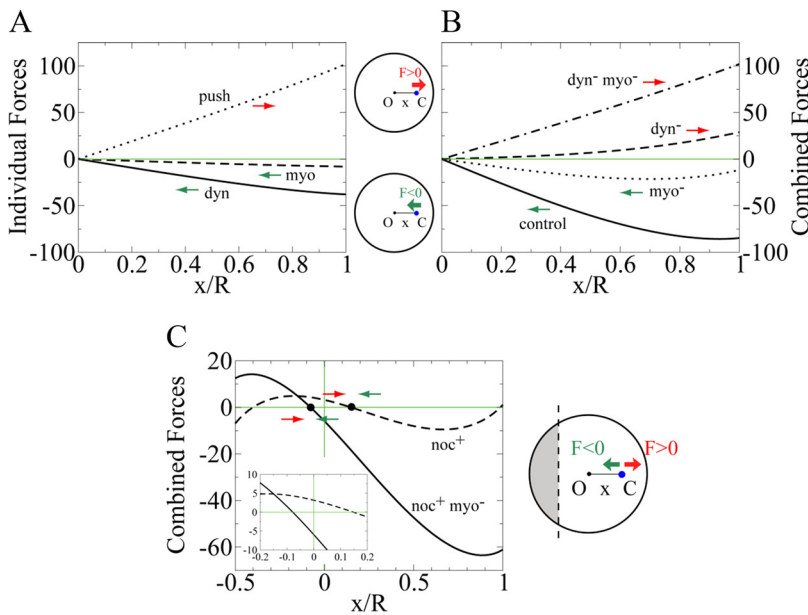


**Figure 3.** Calculated distance dependence of the forces on the CS. Calculated forces on the CS. All distances  $x$  are normalized by the cell radius  $R$ . (A) Normalized net forces on the CS as functions of the normalized distance from the CS to the center (CS shifts to the right side of the center). Solid, dashed, and dotted curves correspond to the dynein, myosin, and pushing forces, respectively. The dynein force is in the unit of  $aL$  (average dynein force per MT;  $a$  is the dynein force per unit length, and  $L$  is the dynamic instability length). The myosin force is in the unit of  $bL^2$  (average actin drag force per MT;  $b$  is the drag force per unit area). The pushing force is in the unit of  $f_{push}$  (average pushing force per MT). (B) The total net force on the CS in units of  $f_{push}$ , in the case when  $aL \approx 3f_{push}$  and  $bL^2 = 8f_{push}$ . Solid line, control cell; dashed line, dynein-inhibited cell; dotted line, myosin-inhibited cell; and dot-dashed line, cell with both dynein and myosin inhibited. (C) In the case when  $aL \approx 3f_{push}$  and  $bL^2 = 8f_{push}$ , the total force on the CS calculated in the nocodazole-affected cell (the nocodazole-affected wedge extends half-way to the center) is shown for the control cell (solid line) and myosin-inhibited cell (dashed line). The inset zooms-in to the region near the cell center to illustrate the signs of the forces there. Black dots show the predicted equilibrium CS positions. Green arrows are centering, inward (negative) forces; red arrows are decentering, outward (positive) forces.

relation illustrates that the stable equilibrium position of the CS is on the left side of the cell center, close to the nocodazole source (Figure 3C, solid). However, because in this situation two weak forces negate a strong force, the net force is weak, and the CS's shift from the center is predicted to be small, in agreement with the experimental observations (Figure 5, A and B). This prediction is further confirmed by the stochastic simulations (Figure 5C and Supplemental Movie 3). When the nocodazole is applied to a myosin-inhibited

cell, the model predicts that the dynein's pulling from the right overwhelms the MTs' pushing at the right. Therefore, with  $aL \approx 3f_{push}$  and  $bL^2 \approx 8f_{push}$ , the application of nocodazole to a myosin-inhibited cell (Figure 3C, dashed) will shift the CS away from the nocodazole source to the right, in agreement with the experiment (Figure 5, D and E). The stochastic simulations (Figure 5F and Supplemental Movie 4) further support this result.

**The Experimental Constraints Allow to Estimate the Forces and Centrosome Mobility in the Centering Mechanism**

All relevant forces, as well as the effective CS drag coefficient, scale with the number of MTs, so the continuous model results are invariant when the MT number changes, adding to the model robustness. However, the stochastic effects of random imbalances that arise from the MT dynamic instability would increase the fluctuation of CS's position when the number of MT decreases. To test the impact of this effect, we used stochastic simulations (Supplemental Movie 1) and observed that when the average MT number is between 30 and 300, the CS stays very close to the center, but with 3 MTs, the CS wandered relatively far from the center (Figure 6A). This allows us to roughly estimate the necessary number of MTs to be  $\sim 100$ . Although accurate experimental count is not possible, this number agrees with our rough image analysis.

In Supplemental Material, we report the calculations that allowed us to use five of six experimental observations discussed above to put stringent constraints on the model parameters (two other observations are explained without such constraints). The model parameter space is simple and two dimensional (Figure 6B). The system behavior is fully determined by two dimensionless ratios: the characteristic dynein force  $aL$  divided by the average pushing force  $f_{push}$  and the characteristic actin-myosin force  $bL^2$  divided by  $f_{push}$ . In this parameter space, there is a relatively narrow triangular region of parameters around the values of  $aL \approx 3f_{push}$  and  $bL^2 \approx 8f_{push}$  (Figure 6B, star), with which the model explains all the experimental observations.

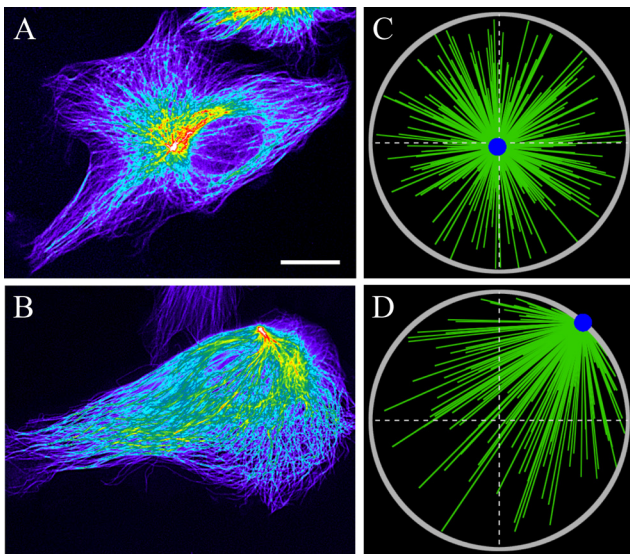


**Figure 4.** Centering in control cells and loss of stability in dynein-inhibited cells. (A) Centered CS in the control cell. (B) CS shifted to the cell edge in the dynein-inhibited cell. Hot-cold colors illustrate high-low tubulin density, respectively. Note that in B, the destabilized CS is at the cell edge closest to the centroid of the cell. Bar, 10  $\mu\text{m}$ . (C) Snapshot of stochastic simulations from Supplemental Movie 1, corresponding to the situation in (A). (D) Snapshot of stochastic simulations from Supplemental Movie 2, corresponding to the situation in B. Gray circle, cell periphery, green lines, MTs; and blue dot, CS.

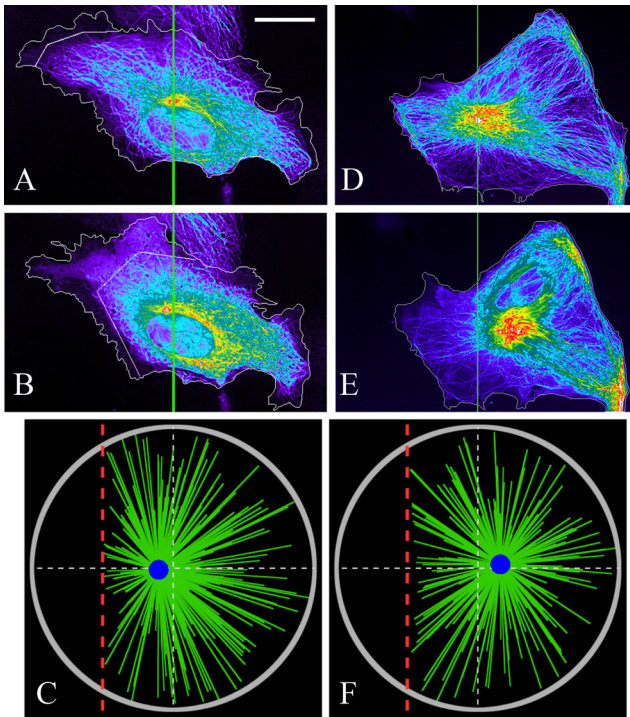


**Figure 5.** Effects of the local nocodazole application on the CS's positioning. Observed CS positions before (A) and after (B) the local nocodazole-application at the left side of the cell. The zigzag line shows the boundary of the nocodazole-affected region. The centrosome shifts slightly toward the nocodazole source, which is in agreement with the model result (C)—the snapshot of the stochastic simulations from Supplemental Movie 3 corresponding to the situation in A and B. (D and E) Observed CS positions before (D) and after (E) the local nocodazole application at the left side of the myosin-inhibited cell. The centrosome shifts slightly away from the nocodazole source, which is in agreement with the model result (F)—the snapshot of the stochastic simulations from Supplemental Movie 4 corresponding to the situation in D and E. Bar, 10  $\mu\text{m}$  (A, B, D, and E), and the colors are the same as those in Figure 4. Red dashed lines indicate the boundary of the nocodazole-affected region in the simulations.

The stringent constraints on the model parameters allow us to estimate the order of magnitude of the characteristic forces on the MTs. When a growing MT runs into an obstacle, it could either undergo catastrophe (Janson *et al.*, 2003) or continue growing by bypassing the obstacle. We assume that these two events occur with comparable possibilities and that the collision-induced catastrophe is a nontrivial part of the total catastrophe events. Then, we estimate that an MT will run into an obstacle about every 30 s, which is roughly the observed characteristic time interval between two catastrophe events (Burakov *et al.*, 2003). We assume that the force is generated for  $\sim 3$  s before the MT starts shortening or bypasses the obstacle and continues growing. Because a stalled MT develops a force of  $\sim 6$  pN (Dogterom and Yurke, 1997), and it takes a few seconds for the stalled MT to start shortening (Janson *et al.*, 2003), the average force on an MT tip would be  $f_{\text{push}} \sim 6 \text{ pN} \times 3 \text{ s} / 30 \text{ s} = 0.6 \text{ pN}$ .

This pushing mechanism is limited by MTs' buckling force, which is the maximal compression force that an MT can sustain. Because the buckling force is inversely proportional to the MT length, it could be very small for long MTs. Indeed, the buckling force for an MT in an aqueous medium can be estimated as  $\sim 10B/l^2$ , where  $B \sim 20 \text{ pN} \times \mu\text{m}^2$  is the

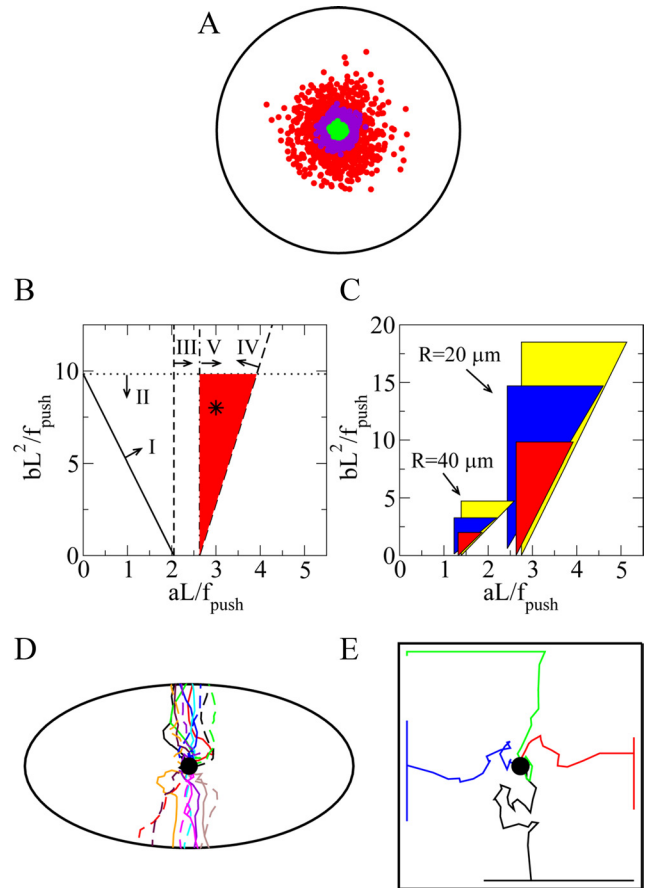


**Figure 6.** Model calibration and predictions. (A) Stochastic simulations illustrate fluctuation of CS position in the control cell with the number of MTs being  $N \sim 300$  (green dots),  $N \sim 30$  (purple dots), and  $N \sim 3$  (red dots). The cell periphery is shown in black. For each case, 1000 simulated CS positions at a 10-min time interval are shown. (B) Parameter values for the disk-like cell with radius  $R = 20 \mu\text{m}$  are shown. Lines and associated arrows indicate domains of the parameter values that support the observed CS behavior in control cell (I), dynein-inhibited cell (II), myosin-inhibited cell (III), cell with the local application of nocodazole (IV), and myosin-inhibited cell with the local application of nocodazole (V). The intersection of these domains shown in red is the region of parameters for which the model explains all experimental observations. This region is around the values determined by the relations  $aL \approx 3f_0$  and  $bL^2 = 8f_0$  shown with the star. (C) Parameter region dependence on the cell shape and size: red regions correspond to circular cells with radius  $R$ ; blue regions to the elliptical cells with the same areas as those of the disk-like cells and an aspect ratio of 2; and yellow regions to the 1D cells with a half-length  $R$ . (D) Trajectories of the CS in a dynein-inhibited ellipsoidal cell from 20 individual stochastic simulations are marked with different colors and line styles. For each trajectory, the CS is initially positioned at the cell center (black dot). (E) Trajectories of the CS in a dynein-inhibited square cell from four individual stochastic simulations are marked with different colors. For each trajectory, the CS is initially positioned at the cell center (black dot). In two simulations, the CS ended at the edge of the cell, and in other two simulations in the corners.

MT flexural rigidity and  $l$  is its length. So, only MTs shorter than  $\sqrt{10B/f_{\text{push}}} \sim 15 \mu\text{m}$  could push effectively. However, the MTs are embedded in an actin elastic gel. This significantly increases the compressive force that the MTs can sustain (Brangwynne *et al.*, 2006): for a long MT embedded into the elastic gel, the buckling length  $\lambda \sim 2\pi (B/Y)^{1/4}$ , where  $Y$  is the Young modulus of the actin meshwork, is

independent of the pushing force and MT length. This length is  $\lambda \sim 2.5 \mu\text{m}$  for characteristic cell cortex elasticity  $Y \sim 10^3 \text{ pN}/\mu\text{m}^2$ . Even for 2 orders of magnitude weaker actin gel that could be above the narrow cortex layer, with  $Y \sim 10 \text{ pN}/\mu\text{m}^2$ , the buckling length remains small,  $\lambda \sim 6 \mu\text{m}$ . Respective buckling force  $\sim 10B/\lambda^2 \sim 6 \text{ pN}$  is well above the characteristic pushing force which therefore will be transduced without weakening to the CS.

Taking into account the estimate of  $aL \approx 3f_{push}$  and  $L \sim 60 \mu\text{m}$ , we conclude that  $a \sim 0.03 \text{ pN}/\mu\text{m}$ . Because a single dynein motor can develop a force of  $\sim 1 \text{ pN}$  (Mallik *et al.*, 2004), there should be an average of  $\sim 1$  pulling dynein motor per  $30 \mu\text{m}$  along an MT, or roughly one working motor per MT. This allows estimating the necessary density of dynein motors in the cortex. We assume that there are  $\sim 100$  MTs in the cell, each being  $\sim 20 \mu\text{m}$  long. Then, there are  $\sim 100 \times 20 \mu\text{m}/30 \mu\text{m} \approx 70$  dynein motors pulling on the MT aster. We further assume that all the dynein motors within  $50 \text{ nm}$  from any MT can associate with that MT (Oiwa and Sakakibara, 2005) and that only half of the motors are pulling. Then, there should be  $\sim 140$  motors localized in an area of  $100 \times 20 \mu\text{m} \times 0.05 \mu\text{m} \approx 100 \mu\text{m}^2$ . Thus, the necessary dynein density is  $\sim 1.5/\mu\text{m}^2$ . Because the area of the cell is  $\pi \times (20 \mu\text{m})^2 \approx 1200 \mu\text{m}^2$ ,  $\sim 2000$  dynein molecules in total have to be in the cortex. We are not aware of any direct experimental measurement of this number; however, existence of hundreds of foci that are likely to contain a few dynein molecules each was reported in Kobayashi and Murayama (2009), which agrees with our prediction.

In Supplemental Material, we estimate the mobility of the MT aster with the CS at the center to be  $\mu \sim 0.03 \mu\text{m}/(\text{pN} \times \text{min})$ , which corresponds to a friction constant of  $\zeta = 1/\mu \sim 30 \text{ pN} \times \text{min}/\mu\text{m}$ . Considering that, when the CS is significantly off-center, a force of  $50f_{push} \sim 30 \text{ pN}$  is applied to the aster, we predict that the CS would shift at speed  $50 \mu f_{push} \sim 1 \mu\text{m}/\text{min}$ , which is the observed moving speed of the CS (Burakov *et al.*, 2003). Note that this is also the characteristic observed speed of the centripetal flow in the flat cells (Alexandrova *et al.*, 2008). We propose that the drag on the MT aster does not originate from the viscous resistance that is negligibly small but instead is from the protein friction (Bormuth *et al.*, 2009) – transient attachments between the MTs and the actin filaments in the cortex. The effective friction constant for each attachment can be estimated as  $\kappa\tau$  (Bormuth *et al.*, 2009), where  $\kappa \sim 10 \text{ pN}/\mu\text{m}$  is the effective spring coefficient of deformed actin filament (Mogilner and Oster, 1996), and  $\tau \sim 1 \text{ s}$  is the characteristic time before such filament detaches from an MT (Howard, 2001). So, the effective friction constant for each attachment is  $\sim 10 \text{ pN} \times \text{s}/\mu\text{m}$ . To account for the total friction constant of  $30 \text{ pN} \times \text{min}/\mu\text{m}$ , we estimate that  $\sim 200$  such attachments, or approximately two attachments per MT, exist in the cell. This number is also a model prediction, because no relevant data have been reported.

#### Centering Mechanism in Cells of Different Shapes and Sizes

Because most of the cells are not perfectly round, we investigated how the centering works in elongated cells (Figure 6D). Our simulations confirmed that all model predictions for the round cells remain valid in the ellipsoidal cells. We also noticed an interesting phenomenon: when dynein is inhibited, the destabilized CS invariably moved to the closest edge of the cell (Figure 6D and Supplemental Movie 5), which is a serendipitous test of the model; when we reexamined the respective images obtained for our previous study (Burakov *et al.*, 2003), we saw that this was exactly the

case (Figure 4B). The explanation stems from the fact that the CS position in this situation is determined only by the force balance between the myosin–actin and pushing forces. The analysis in Supplemental Material shows that the magnitude of the myosin-powered force is very sensitive to the distances in the cell, because the speed of the actin centripetal flow is proportional to the distance from the cell center. Therefore, in the elliptical cell, the myosin–actin force is weaker along the short axis than along the long axis of the cell. On the other hand, the MT pushing force is less affected by the cell geometry, because most of the MT plus-ends are distributed near the CS. Thus, the orientation-insensitive outward pushing overcomes the inward drag from actin flow more easily along the short axis of the cell. Note that very elongated cell is close to a 1D system, for which we have calculated all the forces analytically (see Supplemental Material), which further strengthens the model's predictive power. We also observed that in the elongated and 1D cells, greater ranges of model parameters could explain all experimental observations (Figure 6C) due to subtle distance and angle dependencies of the three principal forces discussed in Supplemental Material. For cells of greater sizes, the parameter region that explains all experimental observations becomes smaller (Figure 6C). The simple reason is that in a large cell, very few MTs could reach the cell boundary, so the dynamic MT probing would work less efficiently.

Cells plated on microfabricated substrates can be forced into particular geometries (Théry *et al.*, 2006). To examine the model-predicted behavior on such cells, we simulated the stochastic force-balance model on the square- (Figure 6E) and fan-shaped (Figure 7) domains mimicking the cells

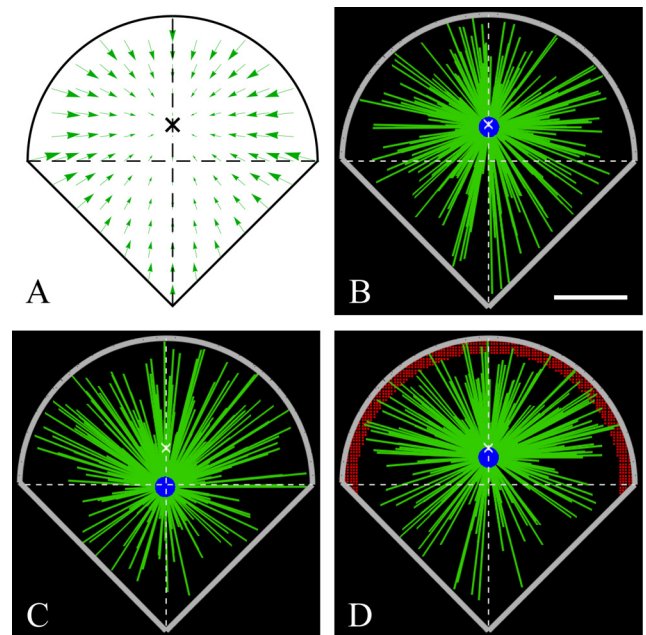


**Figure 7.** Model predictions for the fan-shaped cell. (A) Hypothesized centripetal actin flow field (green arrows) with flow center (cross) near the centroid. (B–D) Snapshots of the simulations with isotropic MT nucleation (B), anisotropic MT nucleation with density of MTs growing toward the round edge being twice the density of MTs growing toward the corner (C), and anisotropic MT nucleation as described in B, but with additional motors at the cell “leading edge” (marked with red dots). Green lines, MTs. Blue circle, CS. Thick gray lines, cell periphery. White crosses, flow center. Bar,  $10 \mu\text{m}$ .

shapes reported in Théry *et al.* (2006). The pattern of the actin centripetal flow in such cells was not observed, so for the square cell we assumed a radially symmetric inward flow, whereas for the fan-shaped cell that resembles motile epithelial cells we chose the flow pattern (Figure 7A) with the convergence point closer to the round edge (and almost at the cell centroid) characteristic for the motile cells. The simulations for the square cell predict, not surprisingly, the stable CS centering (Figure 6E) in agreement with the observations (Théry *et al.*, 2006). Nontrivially, when we switched off dynein force in the simulations, the CS moved to the middle of the cell edge and then either drifted along the edge or went to one of the four cell corners and stayed there (Figure 6E). In the virtual fan-shaped cell, the CS stabilized at the convergence point of the flow (Figure 7B). We investigated what happens if the MT distribution becomes asymmetric, with twice the MTs oriented to the round edge (corresponding to the observed situation in the motile cell where the round edge would be leading). The CS was shifted to the rear (Figure 7C, in agreement with the observations in Théry *et al.*, 2006) due to the dominant effect of the actin retrograde flow near the round edge. The simulations showed that with extra dyneins accumulated at the leading edge of the cell (Figure 7D), the CS shifted toward this edge, similar to what is observed in motile epithelial cells (Dujardin *et al.*, 2003).

#### **Kinesin Pushing along the MT Lengths Can Generate the Decentering Force**

A distinct possibility for the nature of the decentering force is the pushing action of plus-end-directed kinesin motors along the MT lengths (Figure 1F). It is easy to see from comparison between Figure 1, C and F, that the kinesin pushing is opposite to the dynein pulling; other than this, the kinesin and dynein forces would scale similarly with the sizes and distances. Thus, kinesin pushing along the MT lengths can generate the decentering force. In the Supplemental Material, we demonstrate that as far as the total kinesin force in control cells is less than the total dynein force, the kinesin-based mechanism is consistent with all experimental results. However, this mechanism is subject to two requirements. First, kinesin motors should be anchored to stationary structures in the cell, which is possible: binding of kinesin to intermediate filaments have been described previously (Helfand *et al.*, 2004); in addition, conventional kinesin interacts with myosin V, which in turn interacts with actin filaments (Huang *et al.*, 1999). Second, experimental result 4 indicates that the decentering force is switched off if the MTs are stabilized by Taxol. However, kinesin can push the stabilized MTs. Due to this caveat, we favor the hypothesis that it is MT end pushing, rather than kinesin action, that is responsible for the decentering factor. One possibility, however, is that the Taxol-treated MT is mechanically rigid enough so that the kinesin force cannot move the aster off center. Future inhibition of kinesin experiment will be able to resolve this issue.

## **DISCUSSION**

The fundamental questions of whether it is the pushing or the pulling force that positions the nucleus and organelles in cells and what is the origin of this force have been answered in the past decade with a combination of experimental and modeling research (Kimura and Onami, 2005). Here, we used modeling to address this question for the CS centering in the interphase cell (Burakov *et al.*, 2003). The most important result of our study is that in addition to a strong dynein

pulling and a weak myosin-powered actin drag, there is an anticentering pushing force that is generated by the growing MTs throughout the cell. One possible origin for such force is the polymerization ratchet force exerted by the MT plus-ends on obstacles or organelles that are scattered throughout the cell and anchored to the cytoskeletal scaffold (Bjerknes, 1986). Another possibility is that the MTs interact along their lengths with kinesin motors that are anchored to the actin network (Brito *et al.*, 2005). Dynamic MT pushing or pulling on the cell periphery or plus-ends pulling on structures throughout the cell are incompatible with the experiment.

Furthermore, our modeling results argue for the dynein servomechanism—dyneins are anchored to the cortex across the cell and pull on MTs along their lengths—and are inconsistent with the case that dyneins mainly pull on the MT plus-ends from the cell boundary. This conclusion is supported by recent experimental data (Brodsky *et al.*, 2007). By calibrating the model with multiple experimental measurements, we constrain the model parameters to an extent that we are able to predict the order of magnitude of characteristic forces. Namely, we predict that  $\sim 100$  dynamic MTs are responsible for average pushing force of  $\sim 1$  pN per filament. This anticentering force is overwhelmed by a dynein-generated pN-range pulling force on each  $30\text{-}\mu\text{m}$  length of MT and is assisted by a drag force that is caused by 1–2 molecular links between each MT and the centripetally flowing actin network. We also estimate the necessary dynein density to be 1–2 motors per square micron. Finally, we suggest that the viscous-like drag on the shifting CS originates from the dynamic breakage of MT–actin links. We then estimate the CS–MT–aster mobility to be a few hundredths of  $\mu\text{m}/(\text{min} \times \text{pN})$ . We also find that a force of the order of 100 pN is needed to push the aster at a characteristic speed of a few microns per minute, in agreement with Reinsh and Gönczy (1998).

We predict that the centering mechanism is robust: all that is needed for the CS to find the cell center is for total dynein force to be greater than a modest threshold of  $\sim 1$  motor pulling per MT. The experiments and simulations of the nocodazole application demonstrate that significant perturbations of the MT dynamics lead to relatively small shifts of the CS. The reason is the opposing action of dynein and myosin-powered flow on *individual* MTs: whereas dynein pulls an MT outward from the center, the actin flow pulls it inward, so altering the MT distribution leads to changes in the opposing forces that partially cancel each other. Additional indication for the robustness of the centering mechanism is that the CS is predicted to be positioned close to the cell center in square and fan-shaped cells (Figures 6E and 7) in a way insensitive to MTs' anisotropy and system perturbations. The scan of the model parameter space shows that the mechanism becomes even more robust in the elongated cells (Figure 6D)—and in practice, all cells are elongated to some extent. Finally, increasing cell size makes the centering mechanism less robust (Figure 6C), because fewer MTs reach the cell boundaries, in agreement with discussion in Wühr *et al.* (2009). However, a proportional increase of the MT length would restore the centering effectiveness.

The centering mechanism is not only robust but also versatile: the dynein pulling alone can overpower the destabilizing MT pushing to stabilize the CS's centering, so the myosin-powered actin drag seems redundant for the centering. However, the CS's equilibrium point is between the convergence points of the actin centripetal flow and dyneins' pulling field. Therefore, introducing asymmetry and heterogeneity to the two centering forces (by manipulating the dynein and myosin distributions) could shift the CS to a

desired position (Figure 7, B and C). For example, concentrated dyneins at the leading edge of the motile cell could shift the CS toward the front (Figure 7D; Dujardin *et al.*, 2003) against the rearward myosin force (Grabham *et al.*, 2007).

Here, we did not discuss the interactions between the CS and nucleus that are linked intimately to the CS (Robinson *et al.*, 1999) and other elements of cytoskeleton (Starr, 2007). We showed above that the centering is nucleus independent, because the experiments in cell cytoplasts resulted in a similar CS behavior (Burakov *et al.*, 2003). Besides, positions of the nucleus and the CS are established by separate regulatory pathways (Gomes *et al.*, 2005). Nevertheless, mechanical effect of the CS–nucleus interaction is an important future challenge.

The model we proposed is minimal and does not consider factors such as orientation-dependent forces (Tsou *et al.*, 2003), MT length regulation (Tolić-Nørrelykke, 2010), force-velocity properties, and force-driven detachment of dynein (Vogel *et al.*, 2009), and MT bending (Bicek *et al.*, 2009). There are also other positioning processes working in the cell—forceless centering mechanism (Malikov *et al.*, 2005) and cell adhesions determining CS stabilization (Théry *et al.*, 2006), to name but a few. Potentially all these factors are not negligible; future investigations will be needed to see whether they change our model predictions. To further test our force-balance model of centering, suggestions for future experiments include 1) using nanotechnology to build local barriers in the cytoplasm, which would perturb the pushing force and shift the CS in a predictable way; 2) using UV light to locally cancel global nocodazole effect (Hamaguchi and Hiramoto, 1986) to dissect three forces locally; and 3) using laser ablation of MTs to segregate pulling and pushing forces and test the length dependence of the pulling force from dynein (Vogel *et al.*, 2009).

## ACKNOWLEDGMENTS

We thank Dr. Eric Cytrynbaum for help at early stage of this work, Drs. Iva Tolić-Nørrelykke and Ivan Maly for fruitful discussions, and anonymous reviewers for suggestions. This work was supported by National Institute of Health grants GM-068952 (to A.M.) and GM-62290 (to V.R.).

## REFERENCES

Adames, N. R., and Cooper, J. A. (2000). Microtubule interactions with the cell cortex causing nuclear movements in *Saccharomyces cerevisiae*. *J. Cell Biol.* *149*, 863–874.

Alexandrova, A. Y., Arnold, K., Schaub, S., Vasiliev, J. M., Meister, J.-J., Bershadsky, A. D., and Verkhovskiy, A. B. (2008). Comparative dynamics of retrograde actin flow and focal adhesions: formation of nascent adhesions triggers transition from fast to slow flow. *PLoS ONE* *3*, e3234.

Bicek, A. D., Tüzel, E., Demtchouk, A., Uppalapati, M., Hancock, W. O., Kroll, D. M., and Odde, D. J. (2009). Anterograde microtubule transport drives microtubule bending in LLC-PK1 epithelial cells. *Mol. Biol. Cell* *20*, 2943–2953.

Bjerknes, M. (1986). Physical theory of the orientation of astral mitotic spindles. *Science* *234*, 1413–1416.

Bormuth, V., Varga, V., Howard, J., and Schäffer, E. (2009). Protein friction limits diffusive and directed movements of kinesin motors on microtubules. *Science* *325*, 870–873.

Brangwynne, C. P., MacKintosh, F. C., Kumar, S., Geisse, N. A., Talbot, J., Mahadevan, L., Parker, K. K., Ingber, D. E., and Weitz, D. A. (2006). Microtubules can bear enhanced compressive loads in living cells because of lateral reinforcement. *J. Cell Biol.* *173*, 733–741.

Brito, D. A., Strauss, J., Magidson, V., Tikhonenko, I., Khodjakov, A., and Koonce, M. P. (2005). Pushing forces drive the comet-like motility of microtubule arrays in *Dictyostelium*. *Mol. Biol. Cell* *16*, 3334–3340.

Brodsky, I. B., Burakov, A. V., and Nadezhkina, E. S. (2007). Microtubules' interaction with cell cortex is required for their radial organization, but not for centrosome positioning. *Cell Motil. Cytoskeleton* *64*, 407–417.

Burakov, A., Nadezhkina, E., Slepchenko, B., and Rodionov, V. (2003). Centrosome positioning in interphase cells. *J. Cell Biol.* *162*, 963–969.

Burke, B., and Roux, K. J. (2009). Nuclei take a position: managing nuclear location. *Dev. Cell* *17*, 587–597.

Civelekoglu-Scholey, G., and Scholey, J. M. (2010). Mitotic force generators and chromosome segregation. *Cell. Mol. Life Sci.* *67*, 2231–2250.

Dogterom, M., and Leibler, S. (1993). Physical aspects of the growth and regulation of microtubule structures. *Phys. Rev. Lett.* *70*, 1347–1350.

Dogterom, M., and Yurke, B. (1997). Measurement of the force-velocity relation for growing microtubules. *Science* *278*, 856–860.

Dujardin, D. L., and Vallee, R. B. (2002). Dynein at the cortex. *Curr. Opin. Cell Biol.* *14*, 44–49.

Dujardin, D. L., Barnhart, L. E., Stehman, S. A., Gomes, E. R., Gundersen, G. G., and Vallee, R. B. (2003). A role for cytoplasmic dynein and LIS1 in directed cell movement. *J. Cell Biol.* *163*, 1205–1211.

Foethke, D., Makushok, T., Brunner, D., and Nédélec, F. (2009). Force- and length-dependent catastrophe activities explain interphase microtubule organization in fission yeasts. *Mol. Syst. Biol.* *5*, 1–6.

Gomes, E. R., Jani, S., and Gundersen, G. G. (2005). Nuclear movement regulated by Cdc42, MRCK, myosin, and actin flow establishes MTOC polarization in migrating cells. *Cell* *121*, 451–463.

Grabham, P. W., Seale, G. E., Bennecib, M., Goldberg, D. J., and Vallee, R. B. (2007). Cytoplasmic dynein and LIS1 are required for microtubule advance during growth cone remodeling and fast axonal outgrowth. *J. Neurosci.* *27*, 5823–5834.

Grill, S. W., Gönczy, P., Stelzer, E.H.K., and Hyman, A. A. (2001). Polarity controls forces governing asymmetric spindle positioning in the *Caenorhabditis elegans* embryo. *Nature* *409*, 630–633.

Grill, S. W., and Hyman, A. A. (2005). Spindle positioning by cortical pulling forces. *Dev. Cell* *8*, 461–465.

Grishchuk, E. L., Molodtsov, M. I., Ataulkhanov, F. I., and McIntosh, J. R. (2005). Force production by disassembling microtubules. *Nature* *438*, 384–388.

Hamaguchi, M. S., and Hiramoto, Y. (1986). Analysis of the role of astral rays in pronuclear migration in sand dollar eggs by the colcemid-UV method. *Dev. Growth Differ.* *28*, 143–156.

Helfand, B. T., Chang, L., and Goldman, R. D. (2004). Intermediate filaments are dynamic and motile elements of cellular architecture. *J. Cell Sci.* *15*, 133–141.

Holy, T. E., Dogterom, M., Yurke, B., and Leibler, S. (1997). Assembly and positioning of microtubule asters in microfabricated chambers. *Proc. Nat. Acad. Sci. USA* *94*, 6228–6231.

Howard, J. (2001). *Mechanics of Motor Proteins and the Cytoskeleton*, Sunderland, MA: Sinauer Associates.

Huang, J. D., Brady, S. T., Richards, B. W., Stenoi, D., Resau, J. H., Copeland, N. G., and Jenkins, N. A. (1999). Direct interaction of microtubule- and actin-based transport motors. *Nature* *397*, 267–270.

Hwang, E., Kusch, J., Barral, Y., and Huffaker, T. C. (2003). Spindle orientation in *Saccharomyces cerevisiae* depends on the transport of microtubule ends along polarized actin cables. *J. Cell Biol.* *161*, 483–488.

Janson, M. E., de Dood, M. E., and Dogterom, M. (2003). Dynamic instability of microtubules is regulated by force. *J. Cell Biol.* *161*, 1029–1034.

Kimura, A., and Onami, S. (2005). Computer simulations and image processing reveal length-dependent pulling force as the primary mechanism for *C. elegans* male pronuclear migration. *Dev. Cell* *8*, 765–775.

Kobayashi, T., and Murayama, T. (2009). Cell cycle-dependent microtubule-based dynamic transport of cytoplasmic dynein in mammalian cells. *PLoS One* *4*, e7827.

Kodama, A., Karakesisoglou, I., Wong, E., Vaezi, A., and Fuchs, E. (2003). ACF 7, an essential integrator of microtubule dynamics. *Cell* *115*, 343–354.

Koonce, M. P., and Khodjakov, A. (2002). Dynamic microtubules in *Dictyostelium*. *J. Muscle Res. Cell M.* *23*, 613–619.

Malikov, V., Cytrynbaum, E. N., Kashina, A., Mogilner, A., and Rodionov, V. (2005). Centering of a radial microtubule array by translocation along microtubules spontaneously nucleated in the cytoplasm. *Nat. Cell Biol.* *7*, 1213–1218.

- Mallik, R., Carter, B. C., Lex, S. A., King, S. J., and Gross, S. P. (2004). Cytoplasmic dynein functions as a gear in response to load. *Nature* 427, 649–652.
- Manneville, J. B., and Etienne-Manneville, S. (2006). Positioning centrosomes and spindle poles: looking at the periphery to find the centre. *Biol. Cell* 98, 557–565.
- Mikhailov, A. V., and Gundersen, G. G. (1995). Centripetal transport of microtubules in motile cells. *Cell Motil. Cytoskeleton* 32, 173–186.
- Mogilner, A., and Oster, G. (1996). The physics of lamellipodial protrusion. *Eur. Biophys. J.* 25, 47–53.
- Mullins, R. D. (2010). Cytoskeletal mechanisms for breaking cellular symmetry. *Cold Spring Harb. Perspect. Biol.* 2, 1–16.
- O’Connell, C. B., and Wang, Y.-L. (2000). Mammalian spindle orientation and position respond to changes in cell shape in a dynein-dependent fashion. *Mol. Biol. Cell* 11, 1765–1774.
- Oiwa, K., and Sakakibara, H. (2005). Recent progress in dynein structure and mechanism. *Curr. Opin. Cell Biol.* 17, 98–103.
- Paul, R., Wollman, R., Silkworth, W. T., Nardi, I. K., Cimini, D., and Mogilner, A. (2009). Computer simulations predict that chromosome movements and rotations accelerate mitotic spindle assembly without compromising accuracy. *Proc. Nat. Acad. Sci. USA* 106, 15708–15713.
- Pearson, C. G., and Bloom, K. (2004). Dynamic microtubules lead the way for spindle positioning. *Nat. Rev. Mol. Cell Biol.* 5, 481–492.
- Reinsch, S., and Gönczy, P. (1998). Mechanisms of nuclear positioning. *J. Cell Sci.* 111, 2283–2295.
- Robinson, J. T., Wojcik, E. J., Sanders, M. A., McGrail, M., and Hays, T. S. (1999). Cytoplasmic dynein is required for the nuclear attachment and migration of centrosomes during mitosis in *Drosophila*. *J. Cell Biol.* 146, 597–608.
- Rosenblatt, J., Cramer, L. P., Baum, B., and McGee, K. M. (2004). Myosin II-dependent cortical movement is required for centrosome separation and positioning during mitotic spindle assembly. *Cell* 117, 361–372.
- Salmon, W. C., Adams, M. C., and Waterman-Storer, C. M. (2002). Dual-wavelength fluorescent speckle microscopy reveals coupling of microtubule and actin movements in migrating cells. *J. Cell Biol.* 158, 31–37.
- Starr, D. A. (2007). Communication between the cytoskeleton and the nuclear envelope to position the nucleus. *Mol. Biosyst.* 3, 583–589.
- Théry, M., Racine, V., Piel, M., Pépin, A., Dimitrov, A., Chen, Y., Sibarita, J.-B., and Bornens, M. (2006). Anisotropy of cell adhesive microenvironment governs cell internal organization and orientation of polarity. *Proc. Nat. Acad. Sci. USA* 103, 19771–19776.
- Tolić-Nørrelykke, I. M., Sacconi, L., Thon, G., and Pavone, F. S. (2004). Positioning and elongation of the fission yeast spindle by microtubule-based pushing. *Curr. Biol.* 14, 1181–1186.
- Tolić-Nørrelykke, I. M. (2010). Force and length regulation in the microtubule cytoskeleton: lessons from fission yeast. *Curr. Opin. Cell Biol.* 22, 21–28.
- Tran, P., Marsh, L., Doye, V., Inoué, S., and Chang, F. (2001). A mechanism for nuclear positioning in fission yeast based on microtubule pushing. *J. Cell Biol.* 153, 397–412.
- Tsou, M.F.B., Ku, W., Hayashi, A., and Rose, L. S. (2003). PAR-dependent and geometry-dependent mechanisms of spindle positioning. *J. Cell Biol.* 160, 845–855.
- Vogel, S. K., Pavin, N., Maghelli, N., Jülicher, F., and Tolić-Nørrelykke, I. M. (2009). Self-organization of dynein motors generates meiotic nuclear oscillations. *PLoS Biol.* 7, e1000087.
- Wada, M., and Suetsugu, N. (2004). Plant organelle positioning. *Curr. Opin. Cell Biol.* 7, 626–631.
- Weber, K. L., Sokac, A. M., Berg, J. S., Cheney, R. E., and Bement, W. M. (2004). A microtubule-binding myosin required for nuclear anchoring and spindle assembly. *Nature* 431, 325–329.
- Wollman, R., Civelekoglu-Scholey, G., Scholey, J. M., and Mogilner, A. (2008). Reverse engineering of force integration during mitosis in the *Drosophila* embryo. *Mol. Syst. Biol.* 4, 1–13.
- Wühr, M., Dumont, S., Groen, A. C., Needleman, D. J., and Mitchison, T. J. (2009). How does a millimeter-sized cell find its center? *Cell Cycle* 8, 1115–1121.
- Yam, P. T., Wilson, C. A., Ji, L., Hebert, B., Barnhart, E. L., Dye, N. A., Wiseman, P. W., Danuser, G., and Theriot, J. A. (2007). Actin-myosin network reorganization breaks symmetry at the cell rear to spontaneously initiate polarized cell motility. *J. Cell Biol.* 178, 1207–1221.
- Yvon, A.M.C., and Wadsworth, P. (2000). Region-specific microtubule transport in motile cells. *J. Cell Biol.* 151, 1003–1012.

## Supplemental material for Finding the cell center by a balance of dynein and myosin pulling and microtubule pushing: a computational study

Jie Zhu\*, Anton Burakov†, Vladimir Rodionov‡, Alex Mogilner\*.§

\* Department of Neurobiology, Physiology and Behavior and Department of Mathematics, University of California, Davis, CA 95616, USA

† A. N. Belozersky Institute of Physico-Chemical Biology, Moscow State University, Moscow 119899, Russia

‡ Department of Cell Biology and Center for Cell Analysis and Modeling, University of Connecticut Health Center, Farmington, CT 06032, USA

§ Corresponding author. E-mail: mogilner@math.ucdavis.edu

### Distribution of microtubule plus-ends

Microtubules (MTs) in interphase cells grow radially from the centrosome (CS), with plus-ends facing outwards and minus-ends anchored in the CS (see Figure 2A). MTs display dynamic instability, during which they in turn grow steadily with speed  $v_1$  and shorten with speed  $v_2$  (see Figure S1). The MTs switch from the growing to the shortening state with the catastrophe rate  $k_1$ , and from the shortening to the growing state with the rescue rate  $k_2$ . The dynamic instability model we use follows closely the two-state dynamic instability model [1]. We define the densities of the MT plus-ends in the growing and shortening states to be  $\rho_1$  and  $\rho_2$ , respectively. The steady-state distribution of the densities  $\rho_1$  and  $\rho_2$  in two-dimensional (2D) space satisfy the conservation equations:

$$\frac{\partial \rho_1}{\partial t} = -\frac{v_1}{r} \frac{\partial}{\partial r} (r \rho_1) - k_1 \rho_1 + k_2 \rho_2 = 0, \quad (\text{S1})$$

$$\frac{\partial \rho_2}{\partial t} = \frac{v_2}{r} \frac{\partial}{\partial r} (r \rho_2) + k_1 \rho_1 - k_2 \rho_2 = 0, \quad (\text{S2})$$

where  $r$  is the distance from the CS. At the steady state, the outward flux of  $\rho_1$  and the inward flux of  $\rho_2$  should be balanced everywhere, which gives

$$v_1 \rho_1 = v_2 \rho_2. \quad (\text{S3})$$

At CS ( $r = 0$ ), we assume that new MTs are nucleated at a constant rate  $k_0$  from the CS, and that new MTs are always in the growing state. Then, the nucleation rate of growing MTs should balance the extinction rate of shortening MTs. At the steady state,  $k_0$  should be balanced by the flux of  $\rho_2$  into a small circular area  $A$  around the CS with radius  $r \rightarrow 0$ . Let  $\vec{v}_2 = -v_2 \hat{e}_r$  be the velocity vector of the shortening MTs with  $\hat{e}_r$  being the unit radial vector, then the flux balance gives

$$k_0 = -\int_A \nabla \cdot (\vec{v}_2 \rho_2) dA = \int_{\partial A} v_2 \rho_2 dl = 2\pi r v_2 \rho_2, \quad (\text{S4})$$

where  $\partial A$  is the boundary of the area  $A$ ,  $l$  is the length along  $\partial A$ , and the second equality is obtained from Gauss's law. This argument results in the following equation:

$$\rho_2 = \frac{k_0}{2\pi v_2 r} \quad \text{if } r \rightarrow 0. \quad (\text{S5})$$

From Eqs. S1-S5, the steady-state solutions can be found as

$$\rho_1 = \frac{k_0}{2\pi v_1 r} e^{-r/L}, \quad (\text{S6})$$

$$\rho_2 = \frac{k_0}{2\pi v_2 r} e^{-r/L}, \quad (\text{S7})$$

where  $L = v_1 v_2 / (k_1 v_2 - k_2 v_1)$  is the length scale for MT dynamic instability. Equations S6 and S7 describe MTs in an infinite 2D space. Since the distribution of MTs in a cell is limited by the cell membrane, we assume that MTs in the growing state immediately switch to the shortening state when they reach the cell boundary. With this assumption, the flux balance still holds. Therefore, the expressions for  $\rho_1$  and  $\rho_2$  inside the cell are not affected by the existence of the cell boundary.

The concentration of all MT plus-ends in the cell is the sum of  $\rho_1$  and  $\rho_2$ :

$$\rho = \rho_1 + \rho_2 = \frac{k_0}{2\pi v r} e^{-r/L}, \quad (\text{S8})$$

where  $v = v_1 v_2 / (v_1 + v_2)$ . The values of  $v_1$ ,  $v_2$ ,  $k_1$  and  $k_2$  are taken from [2] and are given in Table S1. From the same source, we can glean that the cell radius to be  $R \approx 20 \mu\text{m}$ . Since the total number of MTs in a cell can be calculated as

$$N = 2\pi \int_0^R \rho r dr = \frac{k_0 L}{v} (1 - e^{-R/L}), \quad (\text{S9})$$

we take  $k_0 = 100 \text{ min}^{-1}$ , which corresponds to  $N \approx 300$ . In the continuous deterministic model, we ignore the stochastic effects of the MTs and treat the distribution of the plus-ends of MTs as smooth functions of  $r$  as shown above.

## Force on the centrosome

In a flat disc-like cell with radius  $R$ , we assume that the distance between the CS C and the cell's center O is  $x$  (see Figure 2A). A microtubule CP with length  $r$  is growing toward the cell periphery B. The angle between the MT and the  $x$ -axis is  $\theta$ . We define  $f_x(r, \theta)$  to be the  $x$ -component of force on the CS generated by an individual MT with length  $r$  and orientation  $\theta$ . Because of symmetry, the total force on the CS is simply the integral of  $\rho f_x$  over the entire area of the cell:

$$F_{\text{tot}} = 2 \int_0^\pi d\theta \int_0^{r_m} \rho f_x r dr = \frac{k_0}{\pi v} \int_0^\pi d\theta \int_0^{r_m} f_x e^{-r/L} dr, \quad (\text{S10})$$

where  $r_m$  is the distance from C to the cell periphery at angle  $\theta$ :

$$r_m(\theta) = \text{CB} = \sqrt{R^2 - x^2 \sin^2 \theta} - x \cos \theta. \quad (\text{S11})$$

We consider three possible interaction mechanisms: 1) MTs can be pulled away from the CS by dyneins in the cortex, with force being proportional to MT lengths; 2) MTs can be dragged toward the center of the cell by the actomyosin-driven inward flow of the actin network; and 3) MT growing plus-ends can bump into obstacles in the cortex and push back on the CS. Equation S10 can be expressed as

$$F_{\text{tot}} = F_{\text{dyn}} + F_{\text{act}} + F_{\text{push}}, \quad (\text{S12})$$

where  $F_{\text{dyn}}$ ,  $F_{\text{act}}$  and  $F_{\text{push}}$  are the total forces from dynein, actin-flow drag and MTs' pushing, respectively.

### Mechanism 1: MTs are pulled by the cortex dyneins

Since dyneins in the cell cortex pull the MT along its length in the outward direction, the pulling force  $f_{\text{dyn}}$  on each MT is proportional to  $r$ :

$$f_{\text{dyn}} = ar, \quad (\text{S13})$$

where  $a$  is a constant (dynein force per MT unit length). The force component along the  $x$ -direction is

$$f_x = f_{\text{dyn}} \cos \theta. \quad (\text{S14})$$

Then, Eq. S10 gives

$$F_{\text{dyn}} = -\frac{aL^2k_0}{\pi v} \int_0^\pi (1+u)e^{-u} \cos \theta \, d\theta, \quad (\text{S15})$$

where  $u = r_m/L$ . Eq. S15 can be solved numerically. Figure 3A shows the  $F_{\text{dyn}}-x$  with  $F_{\text{dyn}}$  being normalized by the factor  $aL$ , which is the characteristic dynein force applied to a MT of length  $L$ . For positive  $x$ ,  $F_{\text{dyn}}$  is always negative, and the magnitude of  $F_{\text{dyn}}$  increases with  $x$ . Therefore, the CS is always pushed back toward the cell center, so dynein stabilizes the centering of the CS.

**Mechanism 2: MTs are dragged by the inward flow**

The inward flow of the actin network caused by the actin-myosin contraction produces drag forces on the MTs. The drag force on each segment of a MT is proportional to the velocity of the flow, and is pointing toward the cell's center O. We assume that the actin network's flow speed at a displacement  $\vec{d}$  from point O is proportional to  $-\vec{d}$ :

$$\vec{v}_{\text{flow}}(d) \propto -\vec{d}. \quad (\text{S16})$$

This assumption is in qualitative agreement with experimental observations; it can also be justified with the following argument. In a disc-shaped shell of actin network that is centered at O with radius  $r$  and area  $A = \pi r^2$ , the shrinking rate of the network due to actomyosin contraction is proportional to the amount of myosin inside this region, which is proportional to  $A$ . Therefore, the shrinking rate of this region is

$$-\frac{dA}{dt} \propto A \propto r^2. \quad (\text{S17})$$

The velocity of the inward flow at distance  $r$  from the cell center is simply the shrinking rate of the network radius at  $r$ :

$$v_{\text{flow}} = \left| \frac{dr}{dt} \right| = \left| \frac{dr}{dA} \frac{dA}{dt} \right| \propto r. \quad (\text{S18})$$

For a segment of MT that is at a distance  $s$  from the CS C (see Figure 2A), its displacement from point O is

$$\vec{d}(s) = \vec{x} + s\hat{n}, \quad (\text{S19})$$

where  $\hat{n}$  is the direction of MT growth. We assume that the force density on the segment is proportional to  $\vec{v}_{\text{flow}}$ . From Eq. S16, the total force on the MT is the integral of drag forces on the MT:

$$\vec{f}_{\text{act}} = -b \int_0^r \vec{d} \, ds = -b \left( r\vec{x} + \frac{r^2}{2} \hat{n} \right), \quad (\text{S20})$$

where  $b$  is a constant (drag force per unit area). Then, the value of the force component  $f_x$  is

$$f_x = \vec{f}_{\text{act}} \cdot \hat{e}_x = -b \left( rx + \frac{r^2}{2} \cos \theta \right), \quad (\text{S21})$$

where  $\hat{e}_x$  is the unit vector in the  $x$ -direction. Thus, the total force on the CS can be obtained from Eq. S10 as

$$F_{\text{act}} = -\frac{bL^2xk_0}{v} + \frac{bL^3k_0}{\pi v} \int_0^\pi \left[ \left( 1 + u + \frac{u^2}{2} \right) \cos \theta + \frac{x}{L}(1+u) \right] e^{-u} \, d\theta. \quad (\text{S22})$$

Figure 3A shows the  $F_{\text{act}}-x$  relation with  $F_{\text{act}}$  being normalized by  $bL^2$ , which is the characteristic drag force on a MT of length  $L$  at a distance  $L$  from the cell center. Similar to mechanism 1, for positive values of  $x$ ,  $F_{\text{act}}$  is always negative. Thus, the CS is always pushed by myosin-driven flow toward the center of the cell. This mechanism also stabilizes the CS centering.

**Mechanism 3: growing MTs plus-ends push on structures that are uniformly scattered in the cortex**

Growing MTs can bump into obstacles in the cortex. We assume that the obstacles are evenly distributed in the cortex, and that the average force on each individual growing MT is proportional to the frequency of collisions. Since  $v_1$  is a constant, the frequency of collisions should be the same for all the growing MTs, so the average force on each growing MT should be the same. We define that average force with which each growing MT pushes back on the CS as  $f_{\text{push}}$ . Then the  $x$ -component of the force (see Figure 2A) is

$$f_x = -f_{\text{push}} \cos \theta. \quad (\text{S23})$$

By replacing  $\rho$  with  $\rho_1$  in Eq. S10, the total force on the CS can be obtained as

$$F_{\text{push}} = \frac{f_{\text{push}} L k_0}{\pi v_1} \int_0^\pi e^{-u} \cos \theta \, d\theta. \quad (\text{S24})$$

The normalized  $F_{\text{push}}-x$  relation is shown in Figure 3A. For positive  $x$ ,  $F_{\text{push}}$  is always positive, and the magnitude of  $F_{\text{push}}$  increases as  $x$  increases. Therefore, this force would push the CS away from the cell center and de-stabilize the centering.

### Effects of local application of nocodazole

Figures 2E-F, 3C show the schematics of a cell with a partially cut MT aster by the local application of nocodazole. We assume that the cut is made perpendicular to the  $x$ -axis at  $x = -x_c$  (see Figure S2). Let D be one of the intersections between the cutting line and the cell periphery, the angle between line DC and the  $x$ -axis is

$$\theta_c = \pi - \tan^{-1} \left( \frac{h}{x + x_c} \right), \quad (\text{S25})$$

where  $h = \sqrt{R^2 - x_c^2}$  is the half-length of the cutting line. We define  $r'_m(\theta)$  to be the maximum length of MTs with angle  $\theta$  after the cut is made. It is easy to find that  $r'_m$  satisfies

$$r'_m(\theta) = \begin{cases} r_m(\theta) & \text{if } 0 \leq \theta \leq \theta_c, \\ -(x + x_c) / \cos \theta & \text{if } \theta_c < \theta \leq \pi. \end{cases} \quad (\text{S26})$$

We assume that when the growing MTs reach the cutting line, they immediately convert to the shortening state. Similar to the effect of the cell boundary, the existence of the cutting line does not change the distributions  $\rho_1$  and  $\rho_2$  inside the region that is unaffected by nocodazole. Therefore, the forces on the CS in mechanisms 1–3 can still be obtained from Eqs. S15, S22 and S24 by replacing  $u$  with  $u' = r'_m/L$ :

$$F'_{\text{dyn}} = -\frac{aL^2 k_0}{\pi v} \int_0^\pi (1 + u') e^{-u'} \cos \theta \, d\theta, \quad (\text{S27})$$

$$F'_{\text{act}} = -\frac{bL^2 x k_0}{v} + \frac{bL^3 k_0}{\pi v} \int_0^\pi \left[ \left( 1 + u' + \frac{u'^2}{2} \right) \cos \theta + \frac{x}{L} (1 + u') \right] e^{-u'} \, d\theta, \quad (\text{S28})$$

$$F'_{\text{push}} = \frac{f_{\text{push}} L k_0}{\pi v_1} \int_0^\pi e^{-u'} \cos \theta \, d\theta. \quad (\text{S29})$$

Forces' dependencies on the distance computed with these integrals are shown in Figure S3, A–C. As  $x_c$  decreases, more MTs are cut, force  $F'_{\text{dyn}}$  shifts toward the positive direction because the pulling force along the negative  $x$ -direction is reduced by the cutting of respective MTs. The equilibrium position of the CS also shifts toward the positive  $x$ -direction, which indicates that the CS tends to move away from the nocodazole source.  $F'_{\text{act}}$  shifts to the negative  $x$ -direction for small  $x$ , but to the positive direction at large  $x$ . Therefore, previously centered CS tends to move toward the nocodazole source.  $F'_{\text{push}}$  shifts toward the negative  $x$ -direction, because the opposing forces on MTs in that direction decreases. The CS tends to move toward the nocodazole source.

The overall effect on the CS's positioning should be the sum of all three mechanisms. Although the values of the force constants  $a$ ,  $b$  and  $f_{\text{push}}$  are unknown, their relative magnitudes are constrained by the experimental observations as discussed in the main text.

## Constraints on the parameters from the experimental results

For an initially centered CS in a disc-like cell that is unaffected by nocodazole, forces  $F_{\text{dyn}}$ ,  $F_{\text{act}}$  and  $F_{\text{push}}$  are always zero at  $x = 0$ . Therefore, the CS's direction of motion at  $x = 0$  is determined by the sign of the  $x$ -derivative of the total force. For an initially centered CS in a nocodazole-applied cell, forces  $F'_{\text{dyn}}$ ,  $F'_{\text{act}}$  and  $F'_{\text{push}}$  are non-zero. Thus the CS's direction of motion is determined by the sign of the total force at  $x = 0$ .

*Cell unaffected by nocodazole.* In the control, the CS is stable at the cell center. In our model, this can be formulated as

$$\left( \frac{\partial F_{\text{dyn}}}{\partial x} + \frac{\partial F_{\text{act}}}{\partial x} + \frac{\partial F_{\text{push}}}{\partial x} \right) \Big|_{x=0} < 0. \quad (\text{S30})$$

*Observation 1.* When dynein is inhibited, the CS moves away from the center to the cell periphery. In this case, only mechanisms 2 and 3 contribute to the force. The following should hold:

$$\begin{aligned} \left( \frac{\partial F_{\text{act}}}{\partial x} + \frac{\partial F_{\text{push}}}{\partial x} \right) \Big|_{x=0} &> 0, \\ (F_{\text{act}} + F_{\text{push}})|_{0 < x \leq R} &> 0. \end{aligned} \quad (\text{S31})$$

*Observation 2.* When myosin is inhibited, the CS stays at the center. In this case, only mechanisms 1 and 3 have contributions:

$$\left( \frac{\partial F_{\text{dyn}}}{\partial x} + \frac{\partial F_{\text{push}}}{\partial x} \right) \Big|_{x=0} < 0. \quad (\text{S32})$$

*Observation 3.* When both dynein and myosin are inhibited, the CS moves away from the center. In our model, it can be formulated as

$$\frac{\partial F_{\text{push}}}{\partial x} \Big|_{x=0} > 0. \quad (\text{S33})$$

*Observation 4.* When dynein is inhibited and the dynamics of MTs is inhibited by taxol, the CS stays at the center. This can be expressed as

$$\frac{\partial F_{\text{act}}}{\partial x} \Big|_{x=0} < 0. \quad (\text{S34})$$

*Observation 5.* When nocodazole is applied locally, the CS moves toward the nocodazole source. This indicates

$$(F'_{\text{dyn}} + F'_{\text{act}} + F'_{\text{push}})|_{x=0} < 0. \quad (\text{S35})$$

*Observation 6.* If nocodazole is applied locally to a myosin-inhibited cell, the CS moves away from the nocodazole source. In our model, this shows

$$(F'_{\text{dyn}} + F'_{\text{push}})|_{x=0} > 0. \quad (\text{S36})$$

*Observation 7.* In addition to observation 6, when dynein is weakened by the inhibition of Cdc42, the CS oscillates near the cell center. This can be written as

$$(\epsilon F'_{\text{dyn}} + F'_{\text{push}})|_{x=0} = 0, \quad (\text{S37})$$

where  $0 < \epsilon < 1$  is a factor indicating the weakening of dynein action.

Among the above equations, Eqs. S33 and S34 are always satisfied in our model, and Eq. S37 is similar to Eq. S36. The suitable range of  $aL/f_{\text{push}}$  and  $bL^2/f_{\text{push}}$  for each of the rest of the equations are shown in Figure 6B. The range of parameter values that can satisfy all the experimental observation is the intersection of all those regions. We find that the final range of parameters is simply determined by Eqs. S31, S35 and S36.

Figure 6C shows the ranges of  $aL/f_{\text{push}}$  and  $bL^2/f_{\text{push}}$  that will satisfy all the experimental observations for various cell shapes and sizes. We find that for cells with a similar shape, the suitable range of parameters decreases as the size of the cell increases. For a circular cell, when  $R$  increases from 20  $\mu\text{m}$  to 40  $\mu\text{m}$ , both the maximum and the minimum values of  $aL/f_{\text{push}}$  decrease by a factor of 2, while the maximum value of  $bL^2/f_{\text{push}}$  decreases roughly by a factor of 4. To understand this result, we consider an extreme case where  $L \rightarrow \infty$  and find  $F_{\text{dyn}} \propto aR$ ,  $F_{\text{act}} \propto bR^2$  and  $F_{\text{push}} \propto f_{\text{push}}$ . Indeed, for the case of  $L \rightarrow \infty$ , the term  $e^{-r/L}$  disappears from Eq. S10:

$$F_{\text{tot}} = \frac{k_0}{\pi v} \int_0^\pi d\theta \int_0^{r_m} f_x dr. \quad (\text{S38})$$

For mechanism 1, Eq. S38 becomes

$$F_{\text{dyn}} = \frac{ak_0}{2\pi v} \int_0^\pi r_m^2 \cos \theta d\theta \approx -\frac{aRk_0}{2v} x. \quad (\text{S39})$$

The last term is obtained by approximating  $r_m^2 \approx R^2 - 2xR \cos \theta$  for  $|x| \ll R$ . For mechanism 2, without expanding  $r_m$  near  $x = 0$ , the following relations can be found by keeping only the even terms regarding to  $\theta = \pi/2$ :

$$\int_0^\pi r_m^3 \cos \theta d\theta = -\frac{3\pi}{2} R^2 x, \quad (\text{S40})$$

$$\int_0^\pi r_m^2 d\theta = \pi R^2. \quad (\text{S41})$$

Eq. S38 then gives

$$F_{\text{act}} = -\frac{bk_0}{\pi v} \int_0^\pi \left( \frac{1}{6} r_m^3 \cos \theta + \frac{1}{2} x r_m^2 \right) d\theta = -\frac{bR^2 k_0}{4v} x. \quad (\text{S42})$$

For mechanism 3, by keeping the even terms with respect to  $\theta = \pi/2$ , Eq. S38 becomes

$$F_{\text{push}} = -\frac{f_{\text{push}} k_0}{\pi v_1} \int_0^\pi r_m \cos \theta d\theta = \frac{f_{\text{push}} k_0}{2v_1} x. \quad (\text{S43})$$

This indicates that to keep a certain balance between  $F_{\text{dyn}}$ ,  $F_{\text{act}}$  and  $F_{\text{push}}$ , factors  $a$  and  $b$  should satisfy  $a \propto 1/R$  and  $b \propto 1/R^2$ . We find numerically that this relation still roughly holds if  $L$  is greater than or comparable to  $R$ .

Figure 6C also shows that the suitable range of  $aL/f_{\text{push}}$  and  $bL^2/f_{\text{push}}$  can be affected by the shape of the cells. Given the same cell area, an elliptical cell has a greater range of suitable parameter values than a circular cell has. This is mainly because of the increased maximum value of  $bL^2/f_{\text{push}}$ , which is determined by the dynein-inhibition experiment. In this experiment, if the CS moves away from the center along the short-axis of the cell, the effective size of the cell becomes smaller than  $R$ . From the analysis above, the cell will allow for a higher maximum value of  $bL^2/f_{\text{push}}$ . The shape of the cells affects  $aL/f_{\text{push}}$  in a similar way. The minimum value of  $aL/f_{\text{push}}$  is determined by the nocodazole-application experiment on myosin-inhibited cells. If the nocodazole is applied at one of the pointed ends of the cell, the motion of the CS should be along the long-axis of the cell. Then, the effective size of the cell becomes greater than  $R$ , which results in a decreased minimum value of  $aL/f_{\text{push}}$  as shown in Figure 6C. On the other hand, if the nocodazole is applied at one of the flat sides of the cell, the motion of the CS should be along the short-axis of the cell. If the CS still moves away from the nocodazole source, the effective size of the cell would become smaller than  $R$  and would lead to an increased minimum value of  $aL/f_{\text{push}}$ .

We notice that in our previous study [2], MTs in some cells tend to form parallel patterns along the cell's long-axis. To evaluate the influence of the orientational anisotropy in the distribution of MTs,

we study a one-dimensional (1D) model as an extreme case for all MTs being perfectly aligned. In 1D, Eqs. S1 and S2 become

$$\frac{\partial \rho_1}{\partial t} = -v_1 \frac{\partial \rho_1}{\partial r} - k_1 \rho_1 + k_2 \rho_2 = 0, \quad (\text{S44})$$

$$\frac{\partial \rho_2}{\partial t} = v_2 \frac{\partial \rho_2}{\partial r} + k_1 \rho_1 - k_2 \rho_2 = 0. \quad (\text{S45})$$

Considering the flux balance conditions of  $v_1 \rho_1 = v_2 \rho_2$  for any  $r$  and  $k_0 = v_2 \rho_2$  for  $r \rightarrow 0$ , the solutions of the above equations are

$$\rho_1 = \frac{k_0}{v_1} e^{-r/L}, \quad (\text{S46})$$

$$\rho_2 = \frac{k_0}{v_2} e^{-r/L}. \quad (\text{S47})$$

The total density of plus-ends is

$$\rho = \rho_1 + \rho_2 = \frac{k_0}{v} e^{-r/L}. \quad (\text{S48})$$

Assuming the CS is at  $x$  and the half-length of the cell is  $R$ , the distances from the CS to the left and right cell boundaries are  $R+x$  and  $R-x$ , respectively. For mechanism 1, the total force on the CS is

$$\begin{aligned} F_{\text{dyn}} &= - \int_0^{R+x} \rho r \, dr + \int_0^{R-x} \rho r \, dr = - \frac{ak_0}{v} \int_{R-x}^{R+x} r e^{-r/L} \, dr \\ &= - \frac{aL^2 k_0}{v} [(1+u_1)e^{-u_1} - (1+u_2)e^{-u_2}], \end{aligned} \quad (\text{S49})$$

where  $u_1 = (R-x)/L$  and  $u_2 = (R+x)/L$ . For mechanism 2, similar to the calculations in Eq. S20, the forces on a left-growing and right-growing MT are  $f_L = -b(xr - r^2/2)$  and  $f_R = -b(xr + r^2/2)$ , respectively. Then, the total force on the CS is

$$\begin{aligned} F_{\text{act}} &= \int_0^{R+x} \rho f_L \, dr + \int_0^{R-x} \rho f_R \, dr \\ &= - \frac{bL^2 x k_0}{v} [2 - (1+u_1)e^{-u_1} - (1+u_2)e^{-u_2}] \\ &\quad + \frac{bL^3 k_0}{v} \left[ \left(1 + u_1 + \frac{u_1^2}{2}\right) e^{-u_1} - \left(1 + u_2 + \frac{u_2^2}{2}\right) e^{-u_2} \right]. \end{aligned} \quad (\text{S50})$$

For mechanism 3, the total force is simply

$$F_{\text{push}} = \int_0^{R+x} \rho_1 f_{\text{push}} \, dr - \int_0^{R-x} \rho_1 f_{\text{push}} \, dr = \frac{f_{\text{push}} k_0}{v_1} \int_{R-x}^{R+x} e^{-r/L} \, dr = \frac{f_{\text{push}} L k_0}{v_1} (e^{-u_1} - e^{-u_2}). \quad (\text{S51})$$

When the nocodazole is applied at  $x_c$  on the left of the cell center, the cutting line now becomes the left boundary of the MTs. The distance from the CS to the cut is  $x_c + x$ . By replacing  $u_2$  with  $u_3 = (x_c + x)/L$  in Eqs. S49–S51, one obtains the total forces on the CS with the application of nocodazole. For  $L \rightarrow \infty$ , Eqs. S49–S51 become

$$F_{\text{dyn}} = - \frac{2aRk_0}{v} x, \quad (\text{S52})$$

$$F_{\text{act}} = - \frac{2bk_0}{3v} x^3, \quad (\text{S53})$$

$$F_{\text{push}} = \frac{2f_{\text{push}} k_0}{v_1} x. \quad (\text{S54})$$

The suitable parameter values for a 1D cell are also shown in Figure 6C. The most noticeable difference is that the maximum value of  $bL^2/f_{\text{push}}$  is higher than that of circular or elliptical cells. The reason is that the centering effect from the myosin contraction flow is much weaker in 1D. In a limiting case of  $L \rightarrow \infty$ , we find  $dF_{\text{act}}/dx \propto x^2 \approx 0$  near  $x = 0$ . Therefore, to keep a certain balance between  $F_{\text{act}}$  and  $F_{\text{push}}$ , a higher maximum value of  $b$  is allowed.

Figure 6C allows us to choose suitable values of  $aL/f_{\text{push}}$  and  $bL^2/f_{\text{push}}$ , and then evaluate the motion of the CS under various conditions. For a cell with  $R = 20 \mu\text{m}$ , we choose  $aL/f_{\text{push}} = 3$  and  $bL^2/f_{\text{push}} = 8$ . The total forces on the CS under various conditions are shown in Figure 3, B and F. Once the total force on the CS is found, the CS's motion can be obtained as

$$\frac{dx}{dt} = \mu F_{\text{tot}}, \quad (\text{S55})$$

where  $\mu$  is the mobility of the CS. To estimate the value of  $\mu$ , we consider the following reasoning. We assume that the CS's mobility is determined by the interactions between the MT aster and the actin networks. In mechanism 2, the dragging force on a MT segment of length  $s$  can be written as  $f_s = \zeta_s v_{\text{flow}}$ , where  $\zeta_s$  is the friction constant of the segment. We take  $v_{\text{flow}} = \alpha d$  and  $\zeta_s = \beta s$ , where  $\alpha$  and  $\beta$  are constants. Comparing to Eq. S20, we have  $\alpha\beta = b$ . For the CS, we estimate its friction coefficient to be  $\zeta = \beta l_{\text{tot}}$ , where  $l_{\text{tot}}$  is the total length of all the MTs in the aster:

$$l_{\text{tot}} \approx 2\pi \int_0^R \rho r^2 dr = \frac{k_0 L^2}{v} \left[ 1 - \left( 1 + \frac{R}{L} \right) e^{-R/L} \right]. \quad (\text{S56})$$

The CS's mobility can be written as  $\mu = 1/\zeta = \alpha/b l_{\text{tot}}$ . We take  $\alpha = 0.1 \text{ min}^{-1}$ , which corresponds to a flow rate of  $2 \mu\text{m}/\text{min}$  at a distance of  $20 \mu\text{m}$  from the cell center [3]. For  $b = 8f_{\text{push}}/L^2$ ,  $k_0 = 100 \text{ s}^{-1}$  and  $L = 60 \mu\text{m}$ , we find  $l_{\text{tot}} \approx 3000 \mu\text{m}$  and  $\mu f_{\text{push}} \approx 0.02 \mu\text{m}/\text{min}$ . We estimate  $f_{\text{push}} \sim 0.6 \text{ pN}$  (see main text), then we have  $\mu \sim 0.03 \mu\text{m}/(\text{pN}\cdot\text{min})$ .

## Stochastic simulations

To check our analytical results, we have also performed stochastic simulations in a 2D space. In the simulations, we assume that new MTs are created at the CS at rate  $k_0$  with zero initial lengths and random growth directions, and that each growing MT elongates at speed  $v_1$  until it switches to the shortening state. We treat the switching events as a Poisson process, in which the occurrence of the switching within time  $\tau$  follows a Poisson interval distribution  $P_1(\tau) = k_1 e^{-k_1 \tau}$ . The growth duration  $\tau$  that is associated with each MT is obtained using a random number generator with exponential distribution. Each MT then switches to the shortening state after this particular time. At the shortening state, each MT shortens at velocity  $v_2$  until its length reaches zero. Similar to the calculation of the growth duration, the shortening duration  $\tau$  that is associated with each MT is obtained from the distribution  $P_2(\tau) = k_2 e^{-k_2 \tau}$ . At the end of the shortening state, if the length of the MT remains positive, the MT switches to the growing state again. In addition to these switching events, the cell periphery and the application of nocodazole prevent further elongation of MTs. In the simulations, this effect is treated by immediately switching the MTs into the shortening state when the MTs reach these regions.

The simulation time step is chosen to be smaller than 1/10 of the inverse of the growth/shortening rate, such that on average each growth/shortening state lasts for at least 10 time steps. At each time step, the force on each MT is calculated from our analytical equations (see Eqs. S10 and S15). The total force on the CS is obtained by summing up forces from all the MTs. The motion of the CS is then determined by Eq. S33 in a vector form in 2D.

Our stochastic simulations agree well with the analytical results. In the stochastic simulations, we also find that in a dynein-inhibited elliptical cell, the CS tends to move away from the cell center along

the short-axis of the cell, which agrees with the experimental observations [2]. This can be explained as follows. The motion of the CS in this experiment is determined only by the force balance between the centering force  $F_{\text{act}}$  and the de-centering force  $F_{\text{push}}$ . The magnitude of  $F_{\text{act}}$  is very sensitive to the size of the cell, because the speed of the myosin contraction flow is assumed to be proportional to the distance from the cell center. Therefore, in an elliptical cell,  $F_{\text{act}}$  is weaker along the short-axis than along the long-axis. On the other hand,  $F_{\text{push}}$  is less affected by the geometry of the cell, because most of the growing ends of the MTs are distributed near the CS (see Eq. S6). Thus, the magnitude of  $F_{\text{push}}$  is roughly independent of the CS's moving direction. The combined effect is that the CS is more likely to move away from the cell center along the short-axis of the cell.

## Dynein pulling from the boundary

The experimental observations [2] indicate that dyneins stabilize the centering of the CS. In our model, we treat the force from the dyneins on a MT to be proportional to the length of the MTs. This assumption requires dyneins to be evenly distributed in the cortex. There is another possible dynein-dependent mechanism that can give similar results [4]: pulling from sparsely distributed dyneins at the cell periphery.

If the number of dyneins on the cell periphery is much lower than the number of MTs being in touch with the cell periphery, the pulling force is limited by the availability of dyneins and is therefore independent of the density of MTs. Assuming that  $N_{\text{dyn}}$  dynein molecules are evenly distributed along the cell periphery, the linear density of the dyneins is  $\rho_{\text{dyn}} = N_{\text{dyn}}/2\pi R$ . If each dynein exerts a constant pulling force  $f_1$  on a MT (see Figure S4A, the  $x$ -component of the force is  $f_x = f_1 \cos \theta$ ). It is easy to find  $\cos \theta = (R \cos \varphi - x)/r_m$ , where  $r_m = \sqrt{R^2 + x^2 - 2Rx \cos \varphi}$ . Because of symmetry, the total force from the dyneins on the CS is along the  $x$ -direction:

$$F_{\text{dyn}}^{\text{bnd}} = 2 \int_0^\pi \rho_{\text{dyn}} f_x R d\varphi = \frac{N_{\text{dyn}} f_1}{\pi} \int_0^\pi \frac{R \cos \varphi - x}{r_m} d\varphi. \quad (\text{S57})$$

We used Eq. S57 to find the regions of parameter values (Figure S4B) that satisfy all experimental constraints. We found that these constraints can be satisfied only for  $0 < x_c < R/4$ . This figure indicates that the region of suitable parameters is very sensitive to the value of  $x_c$ , so this mechanism would not be very robust.

Figures S4C and S4D show the  $F$ - $x$  relations for boundary dynein and cortex dynein in nocodazole-affected normal cells, respectively. We focus on the differences near  $x = 0$ , since the CS was initially close to the cell center in the experiment. We can see that as  $x_c$  decreases (nocodazole-affected region increases), force from the cortex dyneins at  $x = 0$  increases evenly, while the force from boundary dyneins increases rapidly at high  $x_c$ , but more slowly at low  $x_c$ . This trend can be seen more clearly in Figure S4E, where the normalized dynein forces at  $x = 0$  are shown as functions of  $x_c$ . At high  $x_c$  (less cut), force from the boundary dynein is significantly higher than that from the cortex dynein, so the CS is more likely to move in the positive  $x$ -direction, which is against the experimental observation. At low  $x_c$  (more cut), force from the boundary dynein is comparable to that from the cortex dynein, therefore the other two mechanisms are able to counteract this force and pull the CS in the negative  $x$ -direction, which agrees with the experiment. Our conclusion is that due to geometric reasons (line versus area), the force from the boundary dyneins is greater than that from the cortex dyneins, especially at high  $x_c$  values. This would make the CS more likely to move away from the nocodazole source, which disagrees with the observations. Therefore, the boundary dynein pulling mechanism requires far more stringent constraints on the model parameters, which makes it less likely.

## Kinesin pushing along the MT lengths

The forces on the CS from kinesins have a similar form as those from dyneins, albeit with an opposite sign and a different prefactor  $c$  indicating different kinesin density and strength. The kinesin force on a MT of length  $r$  can be written as  $f_{\text{kin}} = -cr$ . Since dynein motors produce the centering forces on the centrosome, kinesin motors produce the de-centering forces. We replace the MT pushing mechanism with this kinesin-pushing mechanism, and scale the dynein and myosin forces with  $cL$ . The parameter space satisfying all experimental constraints is shown in Figure S5A. We choose  $aL = 1.2cL$  and  $bL^2 = 3cL$  (star in Figure S5A) and plotted the  $F$ - $x$  relations for the net forces on the CS without (Figure S5B) and with (Figure S5C) nocodazole. These plots show that the kinesin pushing mechanism can have the similar de-centering effect to the MT-pushing action.

## Calculations and results for the square and fan-shaped cells

We introduced the anisotropic and isotropic components of the centripetal actin flow field as follows. The isotropic component is given by the formula

$$\vec{v}_{\text{iso}} = -\alpha\vec{r}, \quad (\text{S58})$$

while the anisotropic one is defined by

$$\vec{v}_{\text{aniso}} = \begin{cases} 0 & \text{if } y \geq 0, \\ \alpha' \left( \frac{y^2}{r^2} \right) \vec{r} & \text{if } y < 0, \end{cases} \quad (\text{S59})$$

where  $\alpha$  and  $\alpha'$  are constants. In the case of the square cell we use just the isotropic flow. For the fan-shaped cell, the net flow is given by (see Figure 7A)

$$\vec{v} = \vec{v}_{\text{iso}} + \vec{v}_{\text{aniso}} = \begin{cases} -\alpha\vec{r} & \text{if } y \geq 0, \\ -\alpha \left[ 1 - g \left( \frac{y^2}{r^2} \right) \right] \vec{r} & \text{if } y < 0, \end{cases} \quad (\text{S60})$$

where  $g = \alpha'/\alpha < 1$  is the reduction factor of the net field at the rear. In the simulations, we choose  $g = 0.5$ .

The total drag force on a MT is the sum of the forces from the flow. Considering a MT with one end at  $\vec{r}_1 = (x_1, y_1)$  and the other at  $\vec{r}_2 = (x_2, y_2)$  (see Figure S6), its length is  $l = |\vec{r}_2 - \vec{r}_1|$  and direction is  $\hat{n} = (n_x, n_y) = (\vec{r}_2 - \vec{r}_1)/l$ . The coordinates of any point on the MT can be expressed as  $\vec{r} = (x, y) = \vec{r}_1 + s\hat{n}$ , where  $s$  is the distance between the point and  $\vec{r}_1$ . The drag force on the MT from field  $\vec{v}_{\text{iso}}$  is

$$\vec{f}_{\text{iso}} = \beta \int_0^l \vec{v}_{\text{iso}} ds = -b \left( l\vec{r}_1 + \frac{l^2}{2} \hat{n} \right), \quad (\text{S61})$$

where  $\beta = b/\alpha$ , as defined previously, is the friction constant per MT length. If the MT is completely in the  $y \geq 0$  region, the drag force from field  $\vec{v}_{\text{aniso}}$  is 0. If it is completely in the  $y < 0$  region, the drag force from field  $\vec{v}_{\text{aniso}}$  is

$$\vec{f}_{\text{aniso}} = \beta \int_0^l \vec{v}_{\text{aniso}} ds = b' \int_0^l \left( \frac{y^2}{r^2} \right) \vec{r} ds, \quad (\text{S62})$$

where  $b' = \alpha'\beta = gb$  and  $y = y_1 + sn_y$ . The  $x$ - and  $y$ -components of  $\vec{f}_{\text{aniso}}$  can be found as

$$f_{\text{aniso},x} = \frac{b'}{2} \{ BC^2 n_x (1 - 4n_y^2) + 2AC^2 n_y (4n_x^2 - 1) + ln_y [ln_x n_y + 2n_x^2 C + 2(n_y^3 x_1 + n_x^3 y_1)] \}, \quad (\text{S63})$$

$$f_{\text{aniso},y} = \frac{b'}{2} [-2AC^2 n_x (1 - 4n_y^2) + BC^2 n_y (4n_x^2 - 1) + ln_y^2 (ln_y + 2y_1 + 4n_x C)], \quad (\text{S64})$$

where  $A$ ,  $B$  and  $C$  are given by

$$A = \tan^{-1} \left[ \frac{n_x y_1 - n_y x_1}{l + n_x x_1 + n_y y_1} \right], \quad (\text{S65})$$

$$B = \ln[l^2 + 2l(n_x x_1 + n_y y_1) + x_1^2 + y_1^2], \quad (\text{S66})$$

$$C = n_x y_1 - n_y x_1. \quad (\text{S67})$$

If the MT is partly in the  $y \geq 0$  region and partly in the  $y < 0$  region, the drag force from field  $\vec{v}_{\text{aniso}}$  acts only on the part that is in the  $y < 0$  region. Then, the total force on the MT is

$$\vec{f} = \vec{f}_{\text{iso}} + \vec{f}_{\text{aniso}}. \quad (\text{S68})$$

If the flow center is not at the origin but at  $(x_{\text{flow}}, y_{\text{flow}})$ , the drag force can be obtained by simply replacing  $(x_1, y_1)$  with  $(x_1 - x_{\text{flow}}, y_1 - y_{\text{flow}})$  in the above equations.

Based on the above force calculations, we performed stochastic simulations in the fan-shaped cell. The main results are described in the main text. Interesting additional results include: (i) when dynein is inhibited, the CS shifts to the sharp corner; (ii) when either myosin is inhibited or nocodazole is applied locally, the CS's shift from the centroid of the cell is not dramatic – the CS remains closer to the centroid than to any of the cell edges.

## References

1. Dogterom M, Leibler S (1993) Physical aspects of the growth and regulation of microtubule structures. *Phys Rev Lett* 70: 1347-1350.
2. Burakov A, Nadezhdina E, Slepchenko B, Rodionov V (2003) Centrosome positioning in interphase cells. *J Cell Biol* 162: 963-969.
3. Yam PT, Wilson CA, Ji L, Hebert B, Barnhart EL, et al. (2007) Actin-myosin network reorganization breaks symmetry at the cell rear to spontaneously initiate polarized cell motility. *The Journal of Cell Biology* 178: 1207-1221.
4. Vallee RB, Stehman SA (2005) How dynein helps the cell find its center: a servomechanical model. *Trends Cell Biol* 15: 288-294.

## Table and Figures

**Table S1. Definition of symbols and parameter values (known values are from Ref. [2]).**

Symbol	Definition	Value
$v_1$	MT's growing velocity	$7.5 \mu\text{m}/\text{min}$
$v_2$	MT's shortening velocity	$16 \mu\text{m}/\text{min}$
$k_1$	Switching rate from growing to shortening state	$2 \text{ min}^{-1}$
$k_2$	Switching rate from shortening to growing state	$4 \text{ min}^{-1}$
$R$	Cell radius	$20 \mu\text{m}$
$L$	length scale for MT dynamic instability	$60 \mu\text{m}$
$k_0$	MT's nucleation rate	$100 \text{ min}^{-1}$
$\rho_1$	Plus-end density of growing MTs	varies
$\rho_2$	Plus-end density of shortening MTs	varies
$\rho$	Plus-end density of all MTs	varies
$x$	Distance between centrosome and cell center	varies
$a$	Dynein's pulling force per unit length	unknown
$b$	Actomyosin's drag force per unit area	unknown
$f_{\text{push}}$	Average pushing force per growing MT	unknown

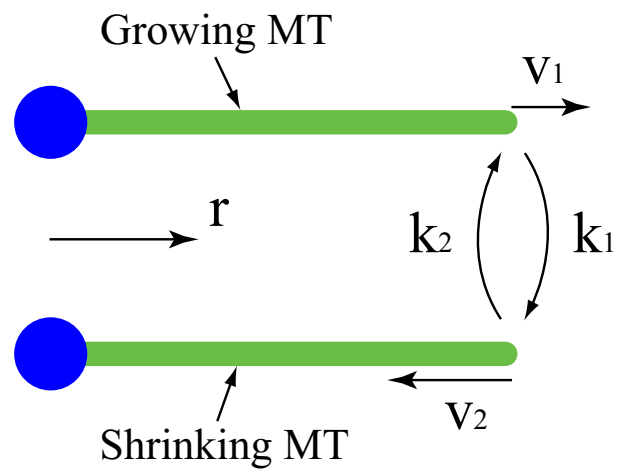


**Figure S1.** Schematic of the dynamics of MTs (green lines). In the growing state, MTs grow with speed  $v_1$  and can switch to the shortening state with rate  $k_1$ . In the shortening state, MTs shorten with speed  $v_2$  and can switch to the growing state with rate  $k_2$ . Blue circles represent the centrosome.

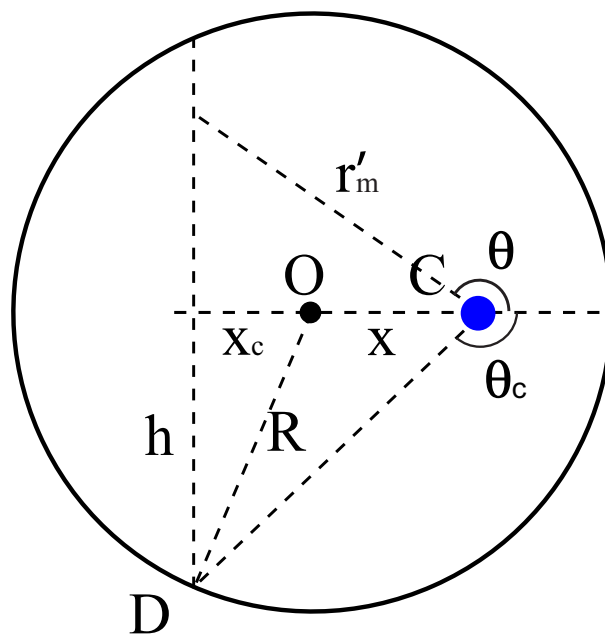


**Figure S2.** Schematic of a cell with nocodazole applied to the left. Blue dot: centrosome.

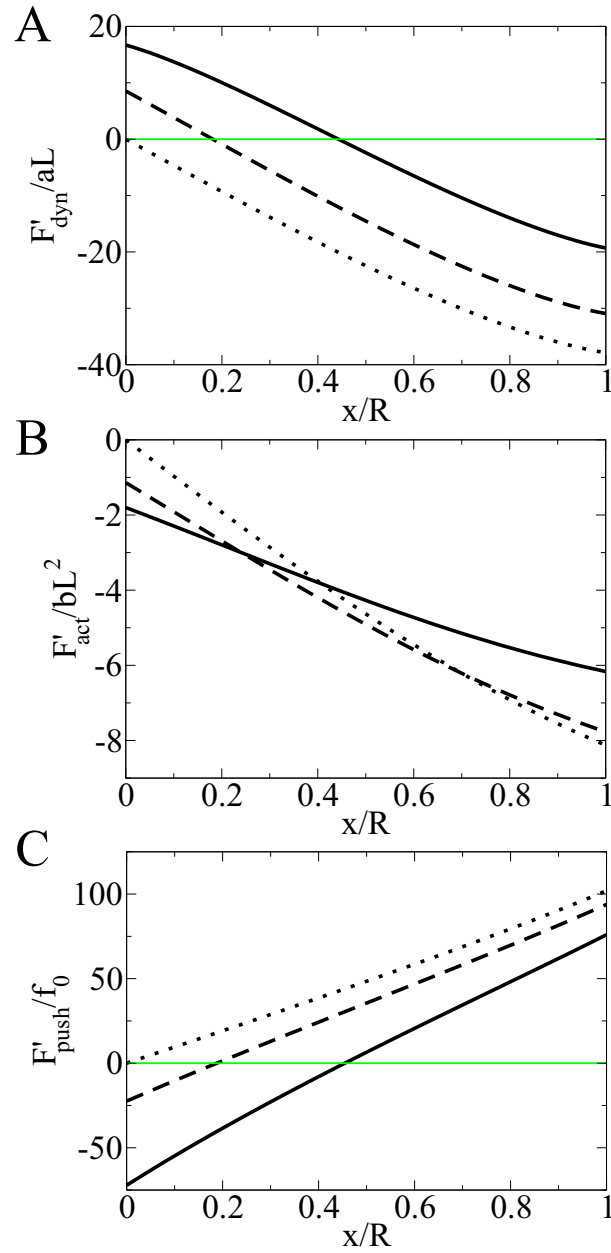


**Figure S3.** (A-C) Normalized forces on the CS from dynein (A), myosin (B) and pushing (C) mechanisms in the nocodazole-treated cell. The normalization of the forces is the same as those in Figure 3A. The dotted lines, for comparison, correspond to the control cell. The dashed lines correspond to the cell with the nocodazole-affected wedge extending half-way to the center. The solid lines correspond to the nocodazole-affected wedge extending all the way to the cell center.

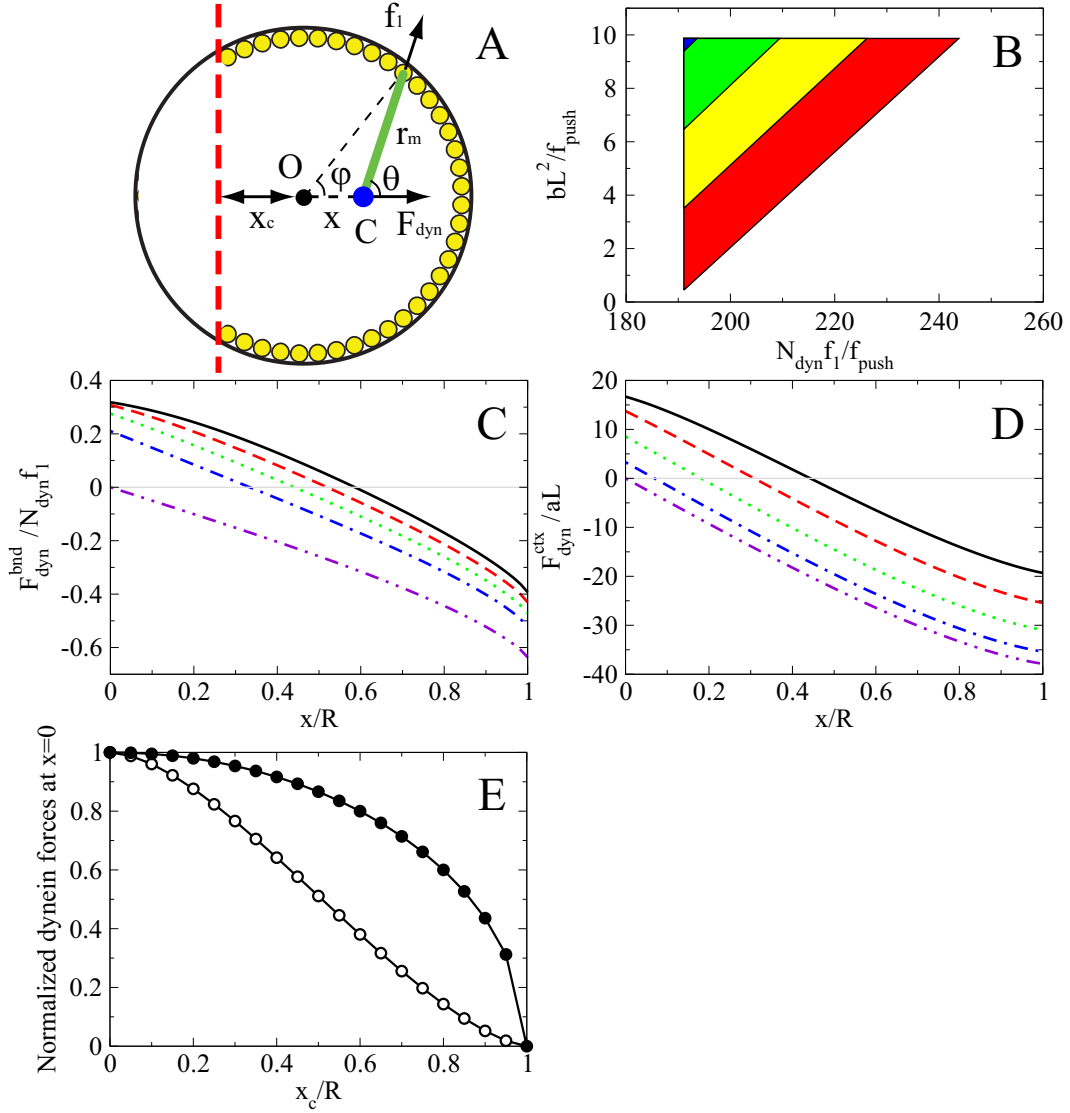


**Figure S4.** Alternative model with dynein molecules sparsely distributed on the cell periphery instead of across the cortex. (A) Schematic of the force calculation. Each dynein molecule (yellow circles) exerts a pulling force  $f_1$  on the CS (blue circle) through MTs (green line). The net force from all the dyneins on the CS is  $F_{\text{dyn}}$ . The nocodazole affected region is on the left side of the red dashed line at the distance  $x_c$  from the cell center. (B) The rectangular parameter regions satisfying all experimental constraints for various values of  $x_c$ . Red:  $x_c = 0.1R$ . Yellow:  $x_c = 0.15R$ . Green:  $x_c = 0.2R$ . Blue:  $x_c = 0.25R$ . Regions for lower values of  $x_c$  are not completely shown since they are covered by others. (C and D)  $x$ -dependence of the net dynein force on the CS, with dyneins located (C) on the cell boundary and (D) across the cortex. Black solid line:  $x_c = 0$ . Red dashed line:  $x_c = 0.25R$ . Green dotted line:  $x_c = 0.5R$ . Blue dot-dashed line:  $x_c = 0.75R$ . Purple dot-dot-dashed line:  $x_c = R$ . (E)  $x_c$ -dependence of the net dynein forces at  $x = 0$ . Solid circles: dyneins on cell boundary. Open circles: across the cortex. Forces are normalized by their maximum values at  $x_c = 0$ .

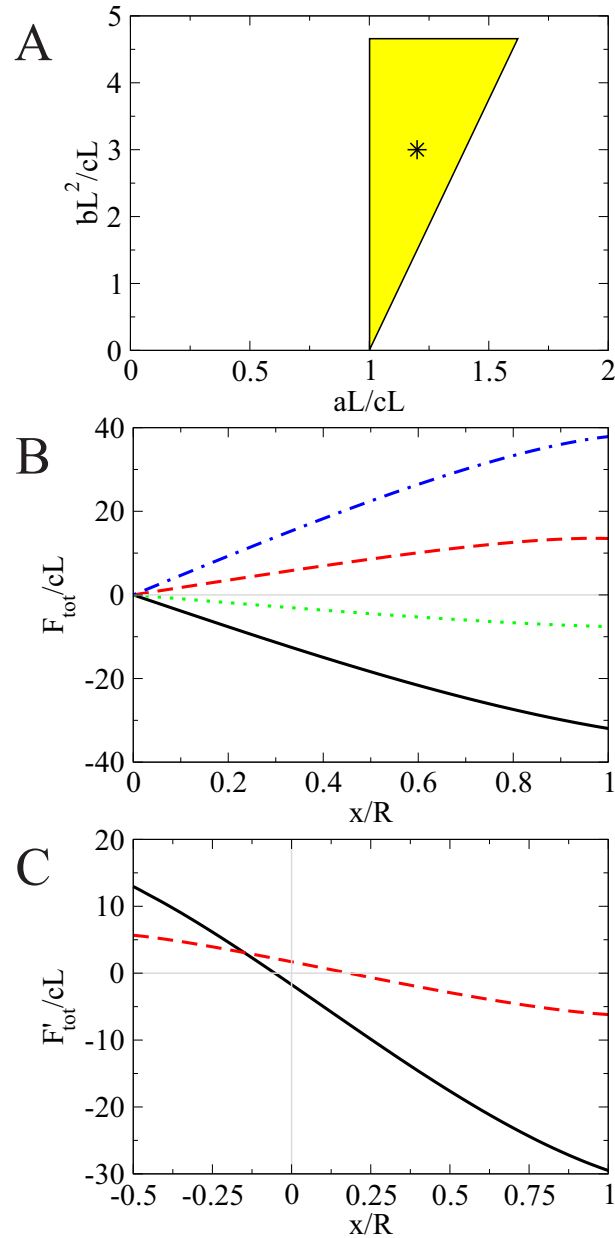


**Figure S5.** Results of the model with dynein and myosin mechanisms as above and alternative kinesin mechanism. (A) Region of suitable parameter values (yellow). The position of the chosen parameters  $aL = 1.2cL$  and  $bL^2 = 3cL$  is shown with the star. (B)  $x$ -dependence of the force on the CS. Solid black line: control cell. Dashed red line: dynein-inhibited cell. Dotted green line: myosin-inhibited cell. Blue dot-dashed line: cell with both dynein and myosin inhibited. (C)  $F$ - $x$  relation for the nocodazole-affected cell (the nocodazole-affected wedge extends half-way to the center). Black solid line: control cell. Red dashed line: myosin-inhibited cell.

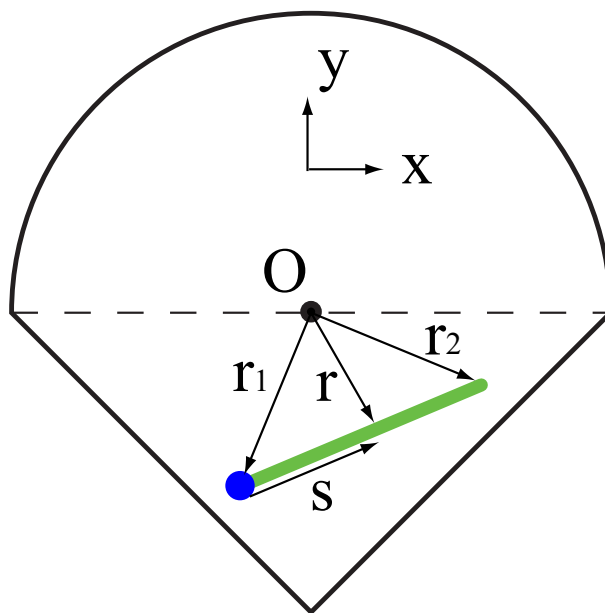


**Figure S6.** Schematic of force calculation in a fan-shaped cell.

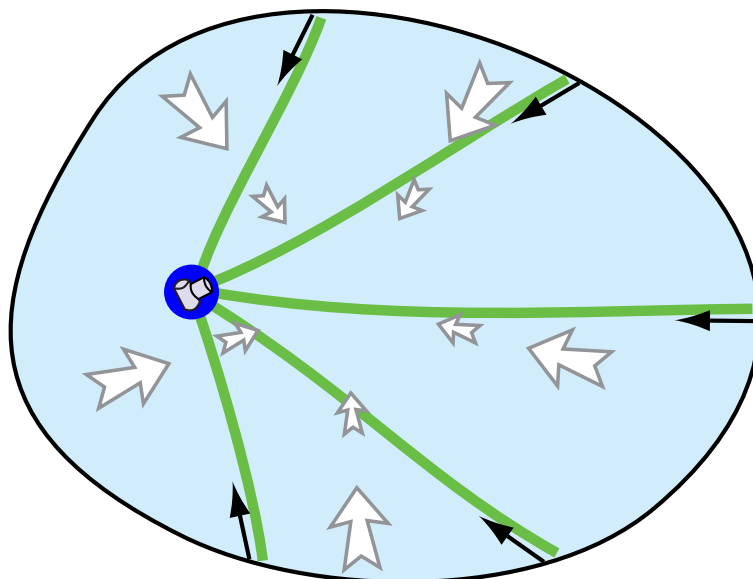


**Figure S7.** If the MT growth is biased to the distal cell edge when the CS shifts away from the center, then both MT pushing on the cell periphery and the actin centripetal flow mechanism destabilize the centering.